Fast search method for Low Frequency Continuous Gravitational Wave Signals

A Thesis

submitted to
Indian Institute of Science Education and Research Pune
in partial fulfillment of the requirements for the
BS-MS Dual Degree Programme

by

Harshit Raj

Indian Institute of Science Education and Research Pune
Dr. Homi Bhabha Road,
Pashan, Pune 411008, INDIA.

April, 2025

Supervisor: Prof. Sanjeev Dhurandhar

Certificate

This is to certify that this dissertation entitled **Fast search method for Low Frequency Continuous Gravitational Wave Signals** towards the partial fulfilment of the BS-MS dual degree programme at the Indian Institute of Science Education and Research, Pune represents study/work carried out by Harshit Raj at Indian Institute of Science Education and Research under the supervision of Prof. Sanjeev Dhurandhar, Professor, IUCAA , during the academic year 2024-2025.

S. V Dhurandhar

Prof. Sanjeev Dhurandhar

Committee:

Prof. Sanjeev Dhurandhar

Prof. Suneeta Vardarajan

This thesis is dedicated to my Parents

Declaration

I hereby declare that the matter embodied in the report entitled **Fast search method for Low Frequency Continuous Gravitational Wave Signals** are the results of the work carried out by me at the IUCAA, Indian Institute of Science Education and Research, Pune, under the supervision of Prof. Sanjeev Dhurandhar and the same has not been submitted elsewhere for any other degree.

Harshit Raj

Harshit Raj

Acknowledgments

I'm grateful to my supervisor, Prof. Sanjeev Dhurandhar, for giving me the opportunity to work under his guidance. His availability, involvement, and invaluable insights have been immensely helpful throughout the project. His mathematical rigor and approach to problem-solving continue to be a constant source of motivation for me.

I sincerely thank Prof. Massimo Tinto (INPE, Brazil), who has unofficially played the role of a co-supervisor. His guidance, discussions, and inputs have been invaluable in shaping this work.

I extend my thanks to Prof. Sanjit Mitra (IUCAA) for his inputs and for being part of the evaluation process. I also thank Prof. Suneeta Vardarajan for coordinating the evaluation process. Additionally, I would like to thank Sudhir Gholap (student, IUCAA) for his assistance with some Python libraries relevant to this work.

I am deeply grateful to my parents for their unwavering support and encouragement. Lastly, I thank my friends at IISER for their everyday conversations, which provided much-needed relaxation and balance.

Abstract

The detection of GW150914 signal from a binary black hole merger marked the beginning of observational gravitational wave astronomy. This has provided us with confidence and insights towards already well-known theory of general relativity. Though the signals from mergers are strong enough to be detected, spinning asymmetric neutron stars are predicted to have quasi monochromatic gravitational waves at very low strain amplitudes. The signals are also frequency modulated due to motion of the detector along with the Earth's rotation and its orbital motion around the Sun. The demodulation requires some correction which depends on the signal parameters. The location of the stars are not known beforehand for most of the cases as most of them don't emit any detectable signals in the electromagnetic spectrum. For example, astrophysically there should be around $\sim 10^9$ neutron stars in our galaxy while only ~ 3000 of them are detected in the electromagnetic spectrum as pulsars. Gravitational wave signals are not yet detected. For an all-sky search, the demodulation is required to be performed over large number of parameter space patches. This makes the search computationally very expensive. In this project, we have explored a method which aims to mitigate the doppler modulations to reduce the number of patches in the parameter space that is required to be searched over. We successfully show that the method is computationally very inexpensive for many relevant cases when compared to other full-coherent search methods. We also show that our method is more sensitive than the earlier methods for low frequency signals given the LIGO detector sensitivity in the $O4$ run.

Contents

List of Figures

Chapter 1

Introduction & Preliminaries

1.1 General Relativity and Gravitational wave solutions

In contrast with Newton's law of gravitation, Einstein's theory of general relativity does not see gravity as a force, but as a curvature in the four dimensional manifold of space-time. Mass and energy are responsible for the curvature and this is governed by the Einstein's equation (1.1)

$$R_{\mu\nu} - \frac{1}{2} g_{\mu\nu} R = 8\pi T_{\mu\nu} \tag{1.1}$$

where, $R_{\mu\nu}$ is the Ricci tensor, R is the Ricci scalar, $g_{\mu\nu}$ is the space-time metric, $T_{\mu\nu}$ is the stress-energy tensor and we are using natural units ($G = 1\,, c = 1$). We can clearly see that curvature described by the terms on the left is determined by mass and energy which is accounted for by the stress-energy tensor.

In the weak field regime, we can write the space-time metric as a perturbation to the flat Minkowski metric

$$g_{\mu\nu} = \eta_{\mu\nu} + h_{\mu\nu}\,,$$

where η is the Minkowski metric with signature $[-1, 1, 1, 1]$ and $|h_{\mu\nu}| \ll 1$.

We introduce trace reverse of $h^{\mu\nu}$

$$\overline{h}^{\mu\nu} = h^{\mu\nu} - \frac{1}{2}\eta^{\mu\nu} h \,, \tag{1.2}$$

h being the trace of $h_{\mu\nu}$, i.e. h^{μ}_{μ}. With this definition and an assumption of Lorenz gauge ($\overline{h}^{\mu\nu}{}_{,\nu} = 0$), we can write Einstein's equation (in linear approximation) as

$$\Box \bar{h}^{\mu\nu} = -16\pi T^{\mu\nu}. \tag{1.3}$$

where $\Box$ is the d'Alembertian operator (four-dimensional Laplacian). Equation (1.3) is called weak field Einstein's equation.

This equation without the source term on the RHS will give solutions for the propagation of gravitational waves. Source free weak field equation is given by

$$\Box \bar{h}^{\mu\nu} = 0 \,, \tag{1.4}$$

whose solutions one can assume to be

$$\bar{h}^{\mu\nu} = A^{\mu\nu} \exp\left(i k_{\mu} x^{\mu}\right) \,. \tag{1.5}$$

This turns out to be solution under condition that k^{μ} is a null vector, i.e. $k^{\mu} k_{\mu} = 0$ (using Minkowski metric). Hence, we can say that gravitational waves travel at the speed of light. Now, exploiting the Lorenz Gauge condition, we can also show that these waves are transverse, i.e. $A^{\mu\nu} k_{\nu} = 0$.

Transverse Traceless Gauge

It can be shown that we can always choose coordinates in which

$$A^{\mu}_{\mu} = 0\,, \tag{1.6}$$

and,

$$A_{\mu\nu}U^{\nu} = 0\,, \tag{1.7}$$

where U is a fixed four-velocity. These conditions define what is called transverse traceless gauge. Now let's consider U such that $U^{\mu} = \delta^{\mu}_{0}$ and consider a wave traveling in the z direction, i.e. $k \equiv \{k\,, 0\,, 0\,, k\}$. With this, we can write A as

$$A^{TT}_{\mu\nu} = \begin{pmatrix} 0 & 0 & 0 & 0 \\ 0 & A_{11} & A_{12} & 0 \\ 0 & A_{21} & -A_{22} & 0 \\ 0 & 0 & 0 & 0 \end{pmatrix}\,, \tag{1.8}$$

with $A_{11} = A_{22}$ and, $A_{12} = A_{21}$. So we can write the wave as a linear combination of two polarizations

$$h^{TT}_{\mu\nu} = h_{+}(t)e^{+}_{\mu\nu} + h_{\times}(t)e^{\times}_{\mu\nu}\,, \tag{1.9}$$

with

$$e^{+}_{\mu\nu} = \begin{pmatrix} 0 & 0 & 0 & 0 \\ 0 & 1 & 0 & 0 \\ 0 & 0 & -1 & 0 \\ 0 & 0 & 0 & 0 \end{pmatrix}\,, \quad e^{\times}_{\mu\nu} = \begin{pmatrix} 0 & 0 & 0 & 0 \\ 0 & 0 & 1 & 0 \\ 0 & 1 & 0 & 0 \\ 0 & 0 & 0 & 0 \end{pmatrix}\,. \tag{1.10}$$

Clearly, $e^{\times}_{\mu\nu}$ and $e^{+}_{\mu\nu}$ are orthogonal, i.e. their scalar product is 0.

Detection from interferometric detectors like LIGO/VIRGO/KAGRA

Current interferometric detectors like LIGO, VIRGO, and KAGRA have two ~ 4 km long arms with free masses (which are mirrors) suspended at their ends. A monochromatic laser beam is split into two using a beam splitter, directing the beams along the two arms of the detector. On their way, the beams pass through a Fabry-Pérot cavity, which increases the effective optical path length, thereby enhancing the detector's sensitivity to small changes in arm length caused by passing gravitational waves. When gravitational wave passes, the proper distance between the masses (mirrors) change differently, causing a variation in the interference pattern of the recombined laser beams. This results in measurable changes in light intensity. The detector's response is given by

$$h(t) = \frac{\delta(L_1) - \delta(L_2)}{L}\,, \tag{1.11}$$

where $\delta(L_1)$ and $\delta(L_2)$ are the changes in the length of the first and the second arm respectively. L is the length of both the arms of the detector.

Now, because the mirrors are free masses suspended at the end of the detectors, the changes in the proper length between them on the passage of gravitational wave is determined by the geodesic equation. For a gravitational wave of the form (1.9), it can be shown that ([4])

$$h(t) = h_{ij}(t)D^{ij}\,, \tag{1.12}$$

where $i, j \in \{1, 2, 3, \cdots\}$ and, D^{ij} is the detector tensor defined as

$$D^{ij} = \frac{1}{2}\left(\hat{\mathbf{e}}^i_{(x)}\hat{\mathbf{e}}^j_{(x)} - \hat{\mathbf{e}}^i_{(y)}\hat{\mathbf{e}}^j_{(y)}\right)\,, \tag{1.13}$$

with $\hat{\mathbf{e}}_{(x)}$ and $\hat{\mathbf{e}}_{(y)}$ being unit vectors in the direction of two of the arms. We finally get

$$h(t) = h_+(t)F_+ + h_\times(t)F_\times \tag{1.14}$$

where,

$$F_+ = \mathbf{e}^+_{ij}D^{ij}, \quad F_\times = \mathbf{e}^\times_{ij}D^{ij}\,. \tag{1.15}$$

F_+ and $F_\times$ are called the antenna pattern functions and are functions of time. This is because the vector pointing towards the arms undergoes rotation with the rotation of the Earth. This is responsible for amplitude modulation of the response signal from continuous gravitational waves.

1.2 Data Analysis

The continuous gravitational waves from spinning neutron stars are expected to create a very weak strain signal on the detectors like LIGO/VIRGO. As a result, they are buried deep in noise. That is why it would require a very long observation time in order to gain desired confidence over its detection. We will be working with excess power method in this analysis which is based on the fact that the power of a monochromatic signal (in the power spectrum) increases as T^2, T being the observation time. while the power of the (white) noise increases linearly with T. This can be shown by Parseval's theorem. Because of this, for a long observation time, power of the signal can stand out compared to the noise power (power signal to noise ratio (SNR) will increase linearly with T).

1.2.1 Discrete Fourier Transform (DFT):

The use of Fourier transform is standard in signal processing. For discrete time series signal, Discrete Fourier transform is used. We use the following definition for discrete Fourier transform for a time series data $\{x_j\}$ of length N, $j \in \{0, 1, 2, \cdots, N-1\}$:

$$\tilde{x}_k = \sum_{j=0}^{N-1} x_j e^{-\frac{2\pi ijk}{N}}. \tag{1.16}$$

where $k \in \{0, 1, 2, \cdots, N-1\}$ and the inverse transform:

$$x_j = \frac{1}{N} \sum_{k=0}^{N-1} \tilde{x}_k e^{\frac{2\pi ijk}{N}}. \tag{1.17}$$

This is the inverse operation of the one in equation 1.16, i.e. taking the DFT of a time series data and then taking the inverse DFT renders back the same time series.

Numerically, Fast Fourier Transform algorithm is used to calculate the DFT (or inverse) for a time (frequency) series signal. The computational cost of the algorithm is of the order of $\mathcal{O}(N \log N)$ (floating point operations (FLOP)) compared to $\mathcal{O}(N^2)$ for brute force DFT calculation.

Power spectrum

The power spectrum of a discrete signal is defined as the magnitude squared of its DFT, i.e.

$$\{P_k\} = \{|\tilde{x}_k|^2\} \tag{1.18}$$

We will refer to P_k sometimes as the power in the k^{th} frequency bin.

Comparison of DFT with Continuous Fourier Transform

Here we see how the quantities like frequency for a continuous Fourier transform are related to the quantities in DFT. A (finite) continuous Fourier transform is defined by:

$$\tilde{x}(f) = \int_0^T x(t)e^{-2\pi ift}\,dt \tag{1.19}$$

,where f is the frequency. Comparing equations (1.16) and (1.19), we see that the analogue to frequency in DFT is

$$f_k = \frac{k}{T} \tag{1.20}$$

Thus the resolution of the frequency in DFT is given by:

$$\Delta f = \frac{1}{T}. \tag{1.21}$$

Monochromatic signal

We take a look at the properties of DFT of a monochromatic signal. For simplicity, let's take the case of a monochromatic signal with frequency $\frac{k_0}{T}$ ($k \in \{0, 1, 2, \cdots, N-1\}$ which is one of the frequencies in (1.20), i.e.

$$x_j = Ae^{\frac{2\pi ijk_0}{N}} \tag{1.22}$$

For this, the Discrete Fourier Transform is given by:

$$\begin{aligned}\tilde{x}_k &= \sum_{j=0}^{N-1} x_j e^{-\frac{2\pi ijk}{N}} \\ &= A\sum_{j=0}^{N-1} e^{-\frac{2\pi ij(k-k_0)}{N}} \\ &= AN\delta_{kk_0}\end{aligned} \tag{1.23}$$

where the third equality is also well known as a property of the sum of all the N^{th} roots of unity.

So it is clear that for a monochromatic signal with frequency one of (1.20) produces a single peak at the corresponding frequency bin in the Fourier domain. When the frequency is not one of (1.20), the power (magnitude of the DFT) is seen to be 'leaking' to adjacent frequency bins. This phenomenon is called spectral leakage. It can be reduced by multiplying the time series data with a tapering window function.

1.2.2 Noise

Noise in the data can be characterized by a stochastic process which is basically a family of random variables $\{n_1, n_2, n_3, \cdots\}$ following a cumulative probability distribution:

$$\mathbf{F}_{1,2,3,\cdots}(a_1, a_2, a_3, \cdots) = P(n_1 \leq a_1, n_2 \leq a_2, n_3 \leq a_3, \cdots) \tag{1.24}$$

,where P denotes the probability.

The first order moment of the probability distribution is given by:

$$\mu_j = \langle n_j \rangle \tag{1.25}$$

where ($\langle\,\rangle$) denotes the ensemble average.

The second order moment is also called as auto correlation function of the distribution, defined as:

$$K(j_1, j_2) = \langle n_{j_1} n_{j_2} \rangle \tag{1.26}$$

Stationary noise

Noise is called strictly stationary if a constant time shift does not change the cumulative probability distribution of the stochastic process which defines it, i.e.

$$\mathbf{F}_{1,2,3,\cdots}(a_1, a_2, a_3, \cdots) = \mathbf{F}_{k+1,k+2,k+3,\cdots}(a_1, a_2, a_3, \cdots) \;\forall\; k \tag{1.27}$$

For stationary noise, the first order moment of the distribution is a constant, i.e.

$$\langle n_j \rangle = \mathit{constant} \;\; \forall\, j \tag{1.28}$$

and the second order moment only depends on the differences in time, i.e. there exists a function $C : \mathbb{Z} \to \mathbb{R}$ (we deal with real noise in the time domain) such that

$$K(j, l) = \langle n_j n_l \rangle = C(j - l). \tag{1.29}$$

Stochastic processes following (1.28 & 1.29) are defined to be **wide sense stationary**.

Power Spectral Density

The power spectrum was defined in equation (1.18). For a noisy time series signal, we deal with the expectation of the power, i.e.

$$\langle |\tilde{n}_k|^2 \rangle = \langle \tilde{n}_k \tilde{n}_k^* \rangle \tag{1.30}$$

For stationary noise this comes out to be:

$$\langle \tilde{n}_k \tilde{n}_k^* \rangle = \mathsf{S}_k \delta_{kk'} \tag{1.31}$$

S_k in (1.31) is called the power spectral density (PSD) of the noise and is related to the Fourier transform of the auto-correlation function.

$$\mathsf{S}_k = N \sum_{j=0}^{N-1} C(j) e^{-\frac{2\pi ijk}{N}} \tag{1.32}$$

So, we can say that for stationary noise, the noise at different frequencies are not correlated. In this work, we will always assume that the noise from the detector is wide sense stationary (i.e. (1.31) holds). At times, when needed and mentioned, we may also assume that the noise is white which means that the power spectral density of the noise is same for all the frequencies. The assumption of white noise is good to consider for a narrow band signal.

One-Sided PSD and the normalized PSD

The one-sided PSD is defined as

$$S_k = 2\,\mathsf{S}_k\,, \tag{1.33}$$

and normalized PSD is defined as

$$\mathbf{S}_k = \frac{S_k}{N}\,. \tag{1.34}$$

The normalized PSD is commonly used in the literature; we will use this while we deal with the depth of the searches. From now on, when we mention PSD, it would mean one-sided PSD unless stated otherwise.

Monochromatic Signal in the Presence of Noise

The correct way to go to calculate the SNR would be to go through detailed probability distributions in the presence and the absence of the signal for given false alarm rate and false dismissal rate but for our purpose of the dependence of the SNR on the time of integration, for a monochromatic signal with frequency $f_k = \frac{k}{T}$,

$$\text{Amplitude } SNR \ \propto \ \sqrt{\frac{P_k}{S_k}} \ \propto \ \sqrt{N} \tag{1.35}$$

P_k being the power of the k^{th} frequency bin of the DFT (in the presence of signal only) of the data and S_k being the power spectral density of the same k^{th} bin.

1.3 The Signal

1.3.1 Signal Frequency

Gravitational wave signals from spinning neutron stars are intrinsically quasi-monochromatic in nature. There are various physical mechanisms that can generate gravitational waves from spinning neutron stars ([11]). As a result there are various possible components of gravitational waves (at different frequencies). In this study, we only consider one component of the signal which is emitted at twice the frequency of the rotation of the star. It has been shown earlier that the problem of detection of each component at different frequency can be dealt independently ([8]). Disregarding the doppler modulations, the signal can be modeled by a monochromatic signal and some spindown parameters taking into account the intrinsic frequency evolution of the signal (an isolated neutron star would slow down as a result of gravitational radiation).

Due to detector's motion with the Earth due to its rotational motion about its own axis and around the sun, we need to take into account the doppler modulations to write the signal that reaches the detector. Let's consider the signal that would reach the solar system barycenter (SSB). The doppler modulations due to constant velocity motion of neutron stars w.r.t. SSB which just shifts the frequency of a monochromatic signal by a constant amount (considering an observation time of one year) and thus, won't affect our data analysis which does not consider any known frequency of the gravitational wave signal. So the frequency of the gravitational wave signal (at the frequency same as that of neutron star's rotation) arriving at SSB can be written as a Taylor series:

$$f_{\mathrm{SSB}}(t) = f_o + \sum_{k=1}^{\infty} \frac{f^{(k)}\tau^k}{k!} \tag{1.36}$$

where τ is time as measured in the SSB frame and $f^{(k)}$s are k^{th} derivatives of frequency measured at $\tau = 0$. f_0 can be absorbed with the frequency derivatives and (1.36) can be written conveniently as:

$$\begin{aligned} f_{\mathrm{SSB}}(\tau) &= f_o\big(1 + \sum_{k=1}^{\infty} \frac{f_k\tau^k}{k!}\big) \\ \text{where, } f_k &= \frac{f^{(k)}}{f_0}\,. \end{aligned} \tag{1.37}$$

Now, the phase of the signal that reaches the SSB at time τ, reaches the detector at time τ' (we ignore any differences between the proper time at SSB and at the detector):

$$\tau' = \tau - \frac{\vec{r}.\hat{n}}{c} \tag{1.38}$$

where $\vec{r}$ is the position vector joining the SSB to the detector, $\hat{n}$ is the unit position vector in the direction of the star (from SSB) and c is the speed of light (propagation of gravitational waves).

We next write the frequency of the signal in detector frame. We'll take into consideration the doppler shift of the frequency due to the motion of the detector relative to SSB within approximation that the speed $|\vec{v}|$ of the detector w.r.t. the SSB is $\ll c$. We'll also ignore the Shapiro delay that arises due to passing of gravitational wave through curved spacetime. These approximations are standard in the literature ([8]).

$$f_{\text{detector}}(t) = f_o\big(1 + \frac{\vec{v}\cdot\hat{n}}{c}\big)\big(1 + \sum_{k=1}^{\infty}\frac{f_k}{k!}\big(t + \frac{\vec{r}.\hat{n}}{c}\big)^k\big) \tag{1.39}$$

As we always deal with signal at detector, we omit the sub-script 'detector' on-wards.

1.3.2 The Phase

The phase of the signal is given by:

$$\Phi(t) = \Phi'_0 + 2\pi\int_0^t f(t)dt \tag{1.40}$$

where Φ'_0 is the initial phase. Now, substituting form equation (1.39) and ignoring all the doppler terms of order two or higher, we get,

$$\Phi(t) = \Phi_0 + 2\pi f_0\big(t + \frac{\vec{r}\cdot\hat{n}}{c} + \sum_{k=1}^{\infty}\frac{f_k t^{k+1}}{(k+1)!} + \frac{\vec{r}\cdot\hat{n}}{c}\sum_{k=1}^{\infty}\frac{f_k t^k}{k!}\big) \tag{1.41}$$

where Φ_0 is the initial phase of the signal (constant). We have dealt with a maximum of one spin down parameter (i.e. $k = 1$) in this work.

Also, we have dealt with signal which is at twice the frequency of the rotation of the neutron star, so the phase of the signal is given by:

$$\Psi(t) = 2\Phi(t) \tag{1.42}$$

So the double frequency signal phase is finally given by

$$\Psi(t) = \Psi_0 + \omega_{\text{gw}}\big(t + \frac{\vec{r}\cdot\hat{n}}{c} + \sum_{k=1}^{\infty}\frac{f_k t^{k+1}}{(k+1)!} + \frac{\vec{r}\cdot\hat{n}}{c}\sum_{k=1}^{\infty}\frac{f_k t^k}{k!}\big) \tag{1.43}$$

where, $\omega_{\text{gw}} = 2\pi f_{gw} = 4\pi f_0$.

The Signal

The strain signal is given by:

$$h(t) = F_+(t)h_+(t) + F_\times(t)h_\times(t) \tag{1.44}$$

where,

$$h_+ = \frac{1}{2}h_0 \sin^2\theta(1+\cos^2 i)\cos\Psi(t), \tag{1.45}$$

$$h_\times = h_0 \sin^2\theta \cos i \sin\Psi(t) \tag{1.46}$$

with i being the angle between the total angular momentum vector of the star and the direction from the Earth to the star & θ is the wobble angle of the star.

F_+ & $F_\times$ are the antenna pattern functions:

$$F_+(t) = \sin\zeta[a(t)\cos 2\psi + b(t)\sin 2\psi] \tag{1.47}$$

$$F_\times(t) = \sin\zeta[b(t)\cos 2\psi - a(t)\sin 2\psi] \tag{1.48}$$

where, $a(t)$ & $b(t)$ were introduced in [8]:

$$\begin{aligned} a(t) = & \frac{1}{16}\sin 2\gamma\,(3-\cos 2\delta)\,(3-\cos 2\theta_l)\cos\left[2\left(\alpha-\phi-\omega_E t\right)\right] \\ & -\frac{1}{4}\cos 2\gamma\sin\theta_l\,(3-\cos 2\delta)\sin\left[2\left(\alpha-\phi-\omega_E t\right)\right] \\ & +\frac{1}{4}\sin 2\gamma\sin 2\theta_l\sin 2\delta\cos\left(\alpha-\phi-\omega_E t\right) \\ & -\frac{1}{2}\cos 2\gamma\cos\theta_l\sin 2\delta\sin\left(\alpha-\phi-\omega_E t\right) \\ & +\frac{3}{4}\sin 2\gamma\cos^2\theta_l\cos^2\delta, \end{aligned} \tag{1.49}$$

$$\begin{aligned} b(t) = & \cos 2\gamma\sin\theta_l\sin\delta\cos\left[2\left(\alpha-\phi-\omega_E t\right)\right] \\ & +\frac{1}{4}\sin 2\gamma\,(3-\cos 2\theta_l)\sin\delta\sin\left[2\left(\alpha-\phi-\omega_E t\right)\right] \\ & +\cos 2\gamma\cos\theta_l\cos\delta\cos\left(\alpha-\phi-\omega_E t\right) \\ & +\frac{1}{2}\sin 2\gamma\sin 2\theta_l\cos\delta\sin\left(\alpha-\phi-\omega_E t\right); \end{aligned} \tag{1.50}$$

where the parameters are as follows:

ζ is the angle between the arms of the detector which we always assume to be $\frac{\pi}{2}$ as it is correct to a good approximation for most of the current detectors like LIGO and VIRGO, ϕ the phase of the rotation of the Earth, θ_l the latitude of the location of the detector, γ the angle between the angle bisectors of the arms of the detector and the east direction, h_0 the amplitude; α, δ & ψ are the angle relating the wave frame to the detector frame (α & δ being the right ascension and declination, while ψ being related to the polarization of the gravitational wave).

We will be dealing with the frequency of gravitational waves at twice the frequency of rotation of the neutron stars, i.e. $f_{gw} = 2f_0$ always holds in this work.

1.4 Data Analysis of gravitational waves from neutron stars

It is clear from (1.39) that the frequency of the signal at the detector is not constant anymore and hence the power in the DFT no longer accumulates in one bin in the power spectrum of the DFT of the data if the change in the frequency of the signal is greater than the frequency resolution of the DFT. We can consider two scenarios to illustrate that this is the case. We won't consider spindown for simplicity.

First consider data collected over a day for GW signal of 200 Hz at a detector located at the equator. In this case, from (1.39), completely ignoring the Earth's motion around the sun, the maximum change in velocity at the equator (w.r.t. SSB) is $\sim 0.93\ Km/s$. Now, consider the neutron star to be located in the plane of the equator of the Earth (i.e. declination 0). Then maximum change in frequency would be $\sim 6.2 \times 10^{-4}\,Hz$ while the resolution of the DFT is $\sim 1.1 \times 10^{-5}\,Hz$ which is smaller than the maximum change in frequency over a day.

Second, consider the orbital motion of the Earth around the SSB for data collected over a year. For this case, the rotational motion can be ignored. Now, considering the star to be located in the plane of the orbit of the Earth, the maximum doppler shift in the frequency is $\sim 4 \times 10^{-2}\ Hz$ while the resolution of the DFT is $\sim 3.3 \times 10^{-8}\ Hz$ which is again much smaller than the shift in frequency.

Demodulation

This frequency modulation is dealt with using a non linear sampling of the signal in time, which is called barycentric sampling ([2]). This sampling depends on the location of the star and other signal parameters like spin-downs. Due to this dependence, one needs to search extensively in the parameter space of the signal. For a full coherent method of data analysis, the number of patches in the parameter space that needs to be searched for grows as a large power of the integration time while the SNR grows only as the square root of the observation time. This makes the data analysis problem of continuous gravitational waves computationally formidable. To deal with this, one needs to rely on semi-coherent methods

([3]) which sums up the powers in shorter segments of the data.

In this work, we explore a full coherent data analysis method for the detection of continuous gravitational waves which seeks to reduce the number of patches in the parameter space that needs to be searched for ([12]) while improving the sensitivity for low-frequency signals.

Chapter 2

Methods and Simulations

We extend and analyze the data analysis method for continuous gravitational waves introduced in [12]. The key idea is that multiplying data separated by approximately six months cancels or reduces the Doppler modulation of the signal. In this chapter, we present the details of methodology and simulations used in our analysis.

2.1 Multiplying the Signals

It can easily be shown that when two (real) signals of different frequencies f_1 & f_2 are multiplied, the resultant signal can be thought of as a superposition of two signals- one at frequency $f_1 + f_2$ and the other at frequency $f_1 - f_2$. Speaking of this in terms of phase, the two components have phases which are sum and difference of phases of the multiplied signals. This is illustrated in (2.1).

$$\cos\Psi_1 \times \cos\Psi_2 = \frac{1}{2}\Big(\cos(\Psi_1 + \Psi_2) + \cos(\Psi_1 - \Psi_2)\Big) \tag{2.1}$$

When we multiply the data separated by $T_{sep} = \frac{\pi}{\Omega}$, the component of the signal with the sum of the phases $\Psi(t)$ &$\Psi(t + T_{sep})$ (1.43) gets the major doppler modulation canceled in case of no spin-downs.

Ignoring the spin-downs,

$$\begin{aligned}\Psi_p(t; T_{sep}) &= \Psi(t) + \Psi(t + T_{sep}) \\ &= 2\Phi_0 + 2\omega_{\text{gw}} t + \omega_{\text{gw}} \frac{(\vec{r}(t) + \vec{r}(t + T_{sep})) \cdot \hat{n}}{c}\end{aligned} \tag{2.2}$$

For $T_{sep} = \frac{\pi}{\Omega}$, the sum of the vectors in (2.2) is:

$$\begin{aligned}\vec{r}(t) + \vec{r}(t + T_{sep}) &= (\vec{r}_{DE}(t) + \vec{r}_{DE}(t + T_{sep})) + (\vec{r}_{ES}(t) + \vec{r}_{ES}(t + T_{sep})) \\ &= \vec{r}_{DE}(t) + \vec{r}_{DE}(t + T_{sep})\end{aligned} \tag{2.3}$$

The second equality follows as a result of cancellation of two vectors in the first line. This holds true for model with Earth revolving the Sun in a circular orbit.

2.1.1 Choice of T_{sep}

$T_{sep} = \frac{\pi}{\Omega}$ so that orbital doppler is completely canceled while there is a residual of rotational doppler

It is evident from (2.3) that with a choice of $T_{sep} = \frac{\pi}{\Omega}$, the orbital doppler which is the dominant component of the doppler modulations over long period of observation times, gets canceled and we are left with modulations of order that comes only due to the rotational motion of the Earth.

Unless otherwise stated, we have always considered $T_{sep} = \frac{\pi}{\Omega}$ in this work.

T_{sep} such that rotational doppler is completely canceled while the orbital doppler has a minimal residual

We explored another choice for T_{sep}. We chose T_{sep} such that the rotational doppler gets completely canceled while there is a minimal residual of the orbital doppler, i.e.

$$\vec{r}_{DE}(t) + \vec{r}_{DE}(t + T_{sep}) = 0 \tag{2.4}$$

For this to happen,

$$T_{sep} = (2N+1)\frac{\pi}{\omega_E} \tag{2.5}$$

where N is any integer. We choose N such that $\vec{r}_{ES}(t) + \vec{r}_{ES}(t + T_{sep})$ is minimized. We don't discuss this further in this chapter for the reasons discussed in Chapter (3).

2.2 Simulations and calculations

We conducted simulations to reassure what happens with the signal in the frequency domain on multiplication in the time domain.

2.2.1 Heterodyning

By Niquist's theorem, we need to sample a signal at least at twice the signal frequency to study its properties in the DFT. But because we need a data for several days at least to study our method and we are limited by computational resources, we used the method of heterodyning to decrease the required sampling rate. By sampling rate we just mean the number of times we need to evaluate the value of analytically simulated signal in one second.

To demonstrate the process of heterodyning we have used, let's assume a simple form of GW signal

$$s(t) = A \sin \Psi(t) \tag{2.6}$$

To heterodyne this signal, we multiply this by another monochromatic signal of frequency f_h. This gives us another signal

$$\begin{aligned} s(t) &= A \sin \Psi(t) \sin 2\pi f_h t \\ &= \frac{A}{2}\{\cos(\Psi(t) - 2\pi f_h t) - \cos(\Psi(t) + 2\pi f_h t)\} \end{aligned} \tag{2.7}$$

We just analytically remove the last higher frequency component from (2.7) and are left with the lower frequency component which is at the difference of frequencies of GW signal and heterodyning signal.

Heterodyning makes sure that frequency modulation is not affected. Suppose the spread in frequency due to Doppler modulation was Δf around frequency f_c. After heterodyning with a frequency of f_h, and only considering the lower frequency part of the heterodyned signal, the spread will again be Δf, but around the frequency $f_c - f_h$. So, now the Niquist's frequency is $2 \times (f_c - f_h)$ instead of $2 \times f_c$. This reduces the computational cost required to test our method of data analysis.

2.2.2 Simplified Models

We work with two simplified models so far. We always consider the Earth to have a circular orbit around the SSB varying the relation between the angular velocities Ω & ω_E. In the first model we consider an integral relation between the two while later on we have relaxed this assumption. We state about these methods ignoring the spin-downs. The spin-downs and its effects are dealt with later when we calculate number of patches in the parameter space that is required to be searched for (section 2.4).

Simple model ($\omega_E = N \times \Omega$; N an odd integer; no spin-downs)

We first conducted some simulations and calculations for an idealized model in which the Earth orbits around the sun in a perfectly circular orbit and the angular velocity of the Earth (ω_E) is an odd integral multiple of the angular velocity (Ω) of its orbital motion around the SSB with the choice of N to be 365. This makes sure that when we multiply the data separated by $T_{sep} = \frac{\pi}{\Omega}$, the doppler modulation gets completely canceled in no spin-down case. The full cancellation of the doppler can be seen from (2.2) & (2.3). The vector sum in (2.3) will completely get canceled for the given case.

So in the case of no spindown, we don't need to search for patches in the parameter space which brings down the computational cost to the same case as that of a directed search.

General model (no particular relation between the angular velocities; no spin-downs)

When we relax the assumption of integral relation between Ω & ω_E we have doppler modulations of the order we would get if the Earth was just rotating about its own axis (no orbital motion).

2.2.3 Noise

We consider the noise to be Gaussian and white which is a good approximation essentially because we are looking at a narrow band signal so that the PSD is approximately constant over the band of a signal. Now, as in our method we multiply two data streams, we can say that we are multiplying two random variables with Gaussian distribution. This product random variable no longer follows a Gaussian distribution ([5]). We investigated the distribution of such a random variable. In the frequency domain though,

$$\tilde{N}_k = \sum_{j=0}^{N-1} N_j e^{-\frac{2\pi ijk}{N}} , \tag{2.8}$$

because of the central limit theorem, we again have a Gaussian noise ([12]). We have numerically tested the validity of this claim also.

2.3 Demodulation

As mentioned in (1.4), we need to demodulate the signal so that the power in the DFT accumulates in one frequency bin only. We use the method of barycentring ([2]) for this. To implement this, we need to sample the data non uniformly in the time domain. How we sample depends on the signal parameters $\{\vec{\lambda}\}$.

Consider a simple model for the signal

$$s(t) = h_0 \cos(\Psi(t)) \tag{2.9}$$

where $\Psi(t)$ is given by (1.43). In order to get the power of the signal accumulated in one frequency bin, we need to resample uniformly in other time coordinates called barycentric time ([2]). This new coordinate is defined as:

$$\begin{aligned} t_b(\vec{\lambda}) &= \frac{\Psi(t;\vec{\lambda})}{\omega_{\text{gw}}} \\ &= t + \frac{\vec{r}\cdot\hat{n}}{c} + \sum_{k=1}^{\infty}\frac{f_k t^{k+1}}{(k+1)!} + \frac{\vec{r}\cdot\hat{n}}{c}\sum_{k=1}^{\infty}\frac{f_k t^k}{k!} \end{aligned} \tag{2.10}$$

In (2.10), we can see that the barycentric resampling will depend on the signal parameters $(\vec{\lambda})$. Generally, as evident from (1.43), these parameters are the sky location parameters (i.e. right ascension and declination) and the spin-down parameters (f_k). So, $\{\vec{\lambda}\} \equiv \{\alpha, \delta, f_1, \cdots\}$. We have considered only one spin-down parameter in this work which is sufficient for the data analysis of slow and old pulsars. Note that the barycentric time does not depend on the GW frequency. This is also true for the product signal.

Product Signal Barycentric Time

We take a look at the component with the summation of the phases as that is the component that matters the most to us. Corresponding to signal like (2.9), the product signal component would be given by:

$$S(t) = \frac{h_0^2}{2}\cos(\Psi(t) + \Psi(t+T_{sep})) \tag{2.11}$$

so that the barycentric time is given by

$$t_b^{prod}(\vec{\lambda}) = \frac{\Psi(t;\vec{\lambda}) + \Psi(t+T_{sep};\vec{\lambda})}{2\omega_{\text{gw}}} \tag{2.12}$$

Note that now we are dividing by twice the GW (angular) frequency as the signal power is concentrated around this (angular) frequency.

Resampling & Patches in the parameter space

Because the sampling rate of LIGO detector is very high compared to the frequency of the gravitational waves that we want to search for, stroboscopic resampling method can be used ([2]). This means that we can still have data sampled at a frequency lower than actual sampling rate of LIGO but still at a significantly higher rate compared to the Niquist's frequency, i.e. twice the maximum GW frequency one is searching for. Now because we have many data samples in between any two samples, we can always look for data sample with a time stamp corresponding to the barycentric time for a particular $\vec{\lambda}$. Though this method does introduce some loss in SNR, it is reliable if the actual sampling rate of the detector is much higher than the Niquist's frequency we need. For example, the sampling rate at LIGO is 16 KHz while the maximum GW signal we search for might be a KHz frequency only. Various methods and implementations of resampling are listed in ([11]). We implement heterodyning in our simulations analytically, so it is exact for a given set of signal parameters.

Now, as the parameters ($\{\vec{\lambda}\}$) are unknown, we need to search over patches in this parameter space, i.e. discrete set of values of $\vec{\lambda}_s$. It is clear that, for a blind search it is nearly impossible to get the search parameters $\vec{\lambda}_s$ to be exactly the same as the signal parameter $\vec{\lambda}$. This mismatch in the parameter while blindly searching over the patches in the parameter space introduces a mismatch in the detected SNR (i.e. fractional loss in the SNR) when compared to the SNR we would have got had we been using $\vec{\lambda}_s \equiv \vec{\lambda}$. As this is impossible to get away with this, signal parameter being unknown, we decide a maximum SNR mismatch we are ready to tolerate. This then decides the size and the number of patches that we need to search over trying to cover the parameter space optimally. For this we define a metric in the parameter space ([1], [2], [7]).

2.4 Parameter space metric and the number of patches

Metric is defined using the loss in the SNR due to usage of patch parameter that is different from the signal parameters. Now, this loss should ideally depend on the data analysis method. For example, we are using barycentric resampling method. But it has been proven that using metric corresponding to this statistic yields similar results for the number of patches as the matched filtering F-statistic leaving the amplitude modulation ([7]). This makes our calculations comparatively simpler than done in ([2]) which requires integrating over barycentric time. We have also conducted comparison for the number of patches in ([2]) corresponding to barycentric resampling method with the one in ([7]) for F-statistic method (see appendix (B)).

Now let's consider extended parameter space including the frequency of the signal

$$\begin{aligned} \{\vec{\Lambda}\} \equiv \{\omega_{\rm gw}, \vec{\lambda}\} &\equiv \{\Lambda^0, \Lambda^1, \Lambda^2, \cdots\} \\ &\equiv \{\Lambda^0, \lambda^1, \lambda^2, \cdots\} \end{aligned} \tag{2.13}$$

Later on, we reduce this parameter space as the FFT algorithm efficiently searches over this parameter at once.

The analytical expression for the phase of the product signal (with $T_{sep} = \frac{\pi}{\Omega}$) in terms of the parameters (just using analytical form of the dot product) is given by (ignoring the constant overall phase)

$$\begin{aligned} \Psi_p(t; \vec{\boldsymbol{\Lambda}}) \approx & 2\omega_{\rm gw} t + \frac{\omega_{\rm gw}}{c} r_p \cos\delta \cos(\omega_E t - \alpha + \tilde{\chi}) \\ & + \frac{\omega_{\rm gw} f_1}{2} \Bigg(2t^2 + 2T_{sep} t + T_{sep}^2 + \frac{2}{c} r_p t \cos\delta \cos(\omega_E t - \alpha + \tilde{\chi}) \\ & + \frac{2T_{sep}}{c} \big(R_E \cos\theta_l \cos\delta \cos(\omega_E t - \alpha + \chi) + R_o \cos\delta \cos(\Omega t - \alpha + \chi') \big) \Bigg) \end{aligned} \tag{2.14}$$

where, $\tilde{\chi}$, χ and, χ' are constant phases independent of $\vec{\Lambda}$. R_o and R_e is the radius of the Earth's orbit around the sun and the radius of the *Earth* respectively and r_p is given by

$$r_p = \sqrt{2R_E^2(1 + \cos\omega_E T)} \cos\theta_l, \tag{2.15}$$

we can, for the purpose of our metric calculation, write this as:

$$
\begin{aligned}
\Psi_p(t;\vec{\mathbf{\Lambda}}) \approx & 2\omega_{\rm gw}t + \frac{\omega_{\rm gw}}{c} r_p \cos\delta\cos(\omega_E t - \alpha + \tilde{\chi}) \\
& + \frac{\omega_{\rm gw} f_1}{2}\left(2t^2 + 2T_{sep}t + T_{sep}^2 + \frac{2T_{sep}}{c}R_o\cos\delta\cos(\Omega t - \alpha + \chi')\right)
\end{aligned}
\tag{2.16}
$$

This approximation is valid because the rotational doppler term in the second expression (with spindown) is negligible compared to the orbital doppler term.

Taking into account the tilt of the Earth's axis

With the tilt of the Earth's axis taken into account, the product signal phase is given by:

$$
\begin{aligned}
\Psi_p(t;\vec{\mathbf{\Lambda}}) \approx & 2\omega_{\rm gw}t + \frac{\omega_{\rm gw}}{c} r_p \cos\delta\cos(\omega_E t - \alpha + \tilde{\chi}) \\
& + \frac{\omega_{\rm gw} f_1}{2}\Bigg(2t^2 + 2T_{sep}t + T_{sep}^2 \\
& + \frac{2T_{sep}}{c}R_o\Big(\cos\alpha\cos\delta\cos\left(\chi' + \Omega t\right) \\
& + \left(\cos\delta\cos\epsilon\sin\alpha + \sin\delta\sin\epsilon\right)\sin\left(\chi' + \Omega t\right)\Big)\Bigg)
\end{aligned}
\tag{2.17}
$$

Notice that it will result in equation 2.16 for $\epsilon = 0$ (as should).

Following the technique in ([6]), we calculate the metric in the parameter space for our method. For the calculation, we required the expression for the phase of the product signal in terms of all parameters $\{\vec{\Lambda}\}$ (2.14 to 2.17). We ignore the tilt of the Earth's axis w.r.t. its orbital plane for ease, i.e. we use equation 2.16 for the phase of the signal in our calculation of the metric. This should not affect the calculation for the number of patches up to order of magnitude. We have tested this claim for the number of patches required to search for in full-coherent searches ([2], [7]) by changing the tilt in the analytical expressions. That calculation was relatively simpler due to the linearized phase approximation ([7]). For our method linearization may not work for large spin-downs as some of the terms are quadratic in the parameters and can not be ignored, unlike the case for full coherent method of ([2]) where such terms can always be ignored.

Similar to (3.6) of ([6]), we define

$$\Psi(t, \vec{\Lambda}, \Delta\vec{\Lambda}) = \Delta\omega_{\mathrm{gw}}\, t + \\ \frac{1}{2}(\Delta f_1 + f_1)\omega_{\mathrm{gw}} \left(2t^2 + 2tT_{sep} + T_{sep}^2 + \frac{2R_o T_{sep}\cos(\Delta\delta + \delta)\cos(\Delta\alpha + \alpha - t\Omega)}{c}\right) \\ + \frac{r_p \omega_{\mathrm{gw}} \cos(\Delta\delta + \delta)\cos(\Delta\alpha + \alpha - t\omega_E)}{c}. \tag{2.18}$$

for a mismatch $\Delta\vec{\Lambda}$ in the template parameters (only up to one spin-down parameter).

Now, the metric elements are defined by

$$g_{ab} = \left\langle \Psi_a \Psi_b \right\rangle - \left\langle \Psi_a \right\rangle \left\langle \Psi_b \right\rangle \tag{2.19}$$

where, $a, b \in \{0, 1, 2, \cdots\}$,

$$\Psi_a \equiv \frac{\partial \Psi}{\partial(\Delta\Lambda^a)}\,, \tag{2.20}$$

and, $\langle\ \rangle$ is the time averaging operator:

$$\langle X \rangle = \frac{1}{T}\int_0^T dt\ X(t)\,. \tag{2.21}$$

The mismatch is (up to second order in $\Delta\vec{\Lambda}$) given by

$$\mu_0 = \sum_{a,b} g_{ab}\ \Delta\Lambda^a\ \Delta\Lambda^b \tag{2.22}$$

Now, as the FFT algorithm searches over all the frequencies readily and cost effectively, what we need is the mismatch minimized over the frequency parameter Λ^0. This results in mismatch given by

$$\mu = \sum_{i,j} \Gamma_{ij} \ \Delta\Lambda^i \ \Delta\Lambda^j \tag{2.23}$$

where, $i, j \in \{1, 2, \cdots\}$ and,

$$\Gamma_{ij} = g_{ij} - \frac{g_{0i}g_{0j}}{g_{00}} \tag{2.24}$$

is the g metric projected orthogonal to the direction of Λ^0 ([6], [2]).

Now that we have the metric, we can calculate the volume of the parameter space

$$V = \int \det(\Gamma) d\vec{\lambda} \tag{2.25}$$

where integral is done over desired ranges of the parameter space $\{\vec{\lambda}\}$. For an all sky search, the sky location will need to be integrated for all possible ranges of right ascension and declination.

Now the number of patches that one need to search for depends on the volume of each patch which depends on the maximum tolerable mismatch $\hat{\mu}$ and the placement of the patches, i.e. the kind of covering that is used. For this, we straightforwardly use the equation (5.18) from ([2]). This is to be noted that there has been improvements in the understanding of optimal placements of the patches ([10]), but we continue to use equation (5.18) from ([2]) for ease in relative comparison.

$$V_{\text{patch}} = \frac{3\sqrt{3}}{4} \left(\frac{4\hat{\mu}}{\dim\{\vec{\lambda}\}} \right)^{\dim\{\vec{\lambda}\}/2} . \tag{2.26}$$

We have calculated the volume of the parameter for two cases. First, for searches with no spin-down, and the second, for searches with one spin-down. We got an analytical expression for the first case while for the second we have numerical results.

2.5 Computational Cost

Now, given the number of patches N_p, we look for the computational cost required to complete the search. For our case, we need to multiply the data, take its DFT using the FFT algorithm, and then find the power spectrum by evaluating the absolute values of the complex numbers in the DFT of the data. We ignore the computational cost required for resampling. This assumption is also considered in ([2]). For a given maximum search frequency f_{max} & observation time T we can find the computational cost in terms of floating point operations that is required to complete all the above calculations.

$$\mathbf{C} = 2N_p f_{max} T + 6 f_{\max} T N_p \left[\log_2\left(2 f_{\max} T\right) + \frac{1}{2}\right] \tag{2.27}$$

where the first term in the RHS of 2.27 is due to the multiplication of N_p different time series signals. The second term corresponds to the computational cost of FFT algorithm and calculating the power spectrum of the DFT. Here we've assumed that the data is sampled at the Niquist's rate $2f_{max}$.

2.6 Sensitivity of the searches

It is good to state the sensitivity of any search in terms of the depth of the search which is defined as

$$\mathcal{D}_{th}(f) = \frac{\sqrt{\mathbf{S}_f}}{h_{th}(f)} \tag{2.28}$$

where, $\mathbf{S}_f$ is the normalized one-sided PSD of the noise of the detector and h_{th} is the minimum amplitude of the signal that is expected to be detected. This is calculated for a fixed false alarm probability (FAP). For our case, we have chosen the FAP to be 1%.

We can also write the depth of a search in terms of a specified False Alarm Probability (FAP) and a fixed False Dismissal Probability (FDP).

Statistics of detection & calculation of depth

The decision of a threshold for detection depends on the probability distribution of the statistic in the presence and in the absence of the signal. Suppose that the detection statistic is ρ; also, suppose that $P_0(\rho)$ is the distribution of the statistic in the absence of the signal while $P_1(\rho)$ is the distribution in the presence of the signal. Now, for a maximum FAP of α, the threshold of the statistic is given by

$$1 - \alpha = \int_0^{\rho_{th}} P_0(\rho) d\rho \tag{2.29}$$

For a real Gaussian noise n_t, the Fourier Transform will also be normally distributed, i.e. both the real and imaginary part of the Fourier transform will be normally distributed.

$$\langle \tilde{n}_f \tilde{n}_f^* \rangle = \langle Re(\tilde{n}_f)^2 \rangle + \langle Im(\tilde{n}_f)^2 \rangle = \frac{S_f}{2} \tag{2.30}$$

where, $\langle\,\rangle$ is ensemble average and S_f is the one-sided power spectral density. By symmetry,

$$\langle Re(\tilde{n}_f)^2 \rangle = \langle Im(\tilde{n}_f)^2 \rangle = \frac{S_f}{4} \, . \tag{2.31}$$

From (2.31), it is clear that

$$\frac{4Re(\tilde{n}_f)^2}{S_f} \quad \& \quad \frac{4Im(\tilde{n}_f)^2}{S_f} \tag{2.32}$$

follow a standard normal distribution. With this motivation, we consider

$$\rho = \frac{4P(f)}{S_f} \tag{2.33}$$

to be our statistic, where $P(f)$ is the power in the bin of the power spectrum of data corresponding to the frequency f (the corresponding bin). ρ follows a central χ^2 distribution. This is because sum of squares of two normally distributed random variable with mean zero follows a central χ^2 distribution. Now we look at the effect of the number of patches on the threshold of the statistic. Remember that we make corrections for N_p number of patches in the parameter space by resampling the data according to the search parameter $\vec{\lambda}_s$. We assume that due to these corrections, the resampled data are statistically independent in all the frequency bins. So, for a search over a maximum frequency of f_{max}, the number of statistically independent realizations is:

$$N_0 = N_p f_{max} T \tag{2.34}$$

, where T is the observation time. Speaking of this, we rewrite (2.29) as

$$1 - \alpha = \left(\int_0^{\rho_{th}} P_0(\rho) d\rho \right)^{N_0} \tag{2.35}$$

Assuming $N_0 \gg 1$ and using binomial expansion up to first term, we get

$$\begin{gathered} \frac{\alpha}{N_0} = \int_{\rho_{th}}^{\infty} P_0(\rho) d\rho \\ \text{where,} \\ P_0 \sim \chi^2(2, 0) \end{gathered} \tag{2.36}$$

is the χ^2 distribution with 2 degrees of freedom and non-centrality parameter 0. This is same as the exponential distribution

$$P_0(\rho) = \frac{1}{2} e^{-\frac{\rho}{2}} , \tag{2.37}$$

which on substitution in (2.36), gives

$$\rho_{th} = 2 \ln \left(\frac{N_0}{\alpha} \right) . \tag{2.38}$$

Depth of the full coherent search

Now we calculate the minimum amplitude of a monochromatic signal that is expected to be detected following ([2]). For current purposes, we'll also ignore the details of amplitude modulation as that can be dealt with using other methods like F statistic ([8]). Assume a monochromatic signal

$$h(t) = h_0 \cos(2\pi f_{gw} t) \tag{2.39}$$

in the presence of Gaussian noise with (one-sided) PSD S_f. If the signal is present, the expected power (in the signal) given that the statistic is ρ_{th} is $\frac{S_f}{2}(\rho_{th}-1)$. This is because the expected power in the noise is given by twice the one-sided PSD. So, the threshold amplitude of the signal is given by

$$\frac{h_{th}^2 T^2}{2} = \frac{S_f}{2}(\frac{\rho_{th}}{2} - 1)\,. \tag{2.40}$$

So we get the depth of the full-coherent search as

$$\mathcal{D}_{th}(f) = \frac{\sqrt{\mathbf{S}_f}}{h_{th}(f_{gw} = f)} = \sqrt{\frac{T}{\frac{\rho_{th}}{2} - 1}} \tag{2.41}$$

Depth of the product signal search

Let's assume GW signal of form:

$$h(t) = h_0 \cos(\Psi(t)) \tag{2.42}$$

The product signal component near double the frequency of the GW signal (let's consider that the original signal has frequency near f_{gw}) is given by:

$$h^{prod}(t) = \frac{h_0^2}{2}\cos(\Psi(t) + \Psi(t + T_{sep})) \tag{2.43}$$

We see that for our method the change is in the amplitude of the signal and the PSD of the noise. The PSD of the product noise is the square of the PSD of the noise ([5]). So with these changes, the detection depth is given by

$$\mathcal{D}_{th}^{prod}(2f) = \frac{\sqrt{\mathbf{S}_{2f}}}{h_{th}^{prod}(f_{gw} = f)} = \frac{1}{\sqrt{2}}\left(\frac{T}{\frac{\rho_{th}}{2} - 1}\right)^{\frac{1}{4}} \tag{2.44}$$

where ρ_{th} is calculated using (2.36) and, the first equality can be considered as a definition. It should be noted that in (2.44), the depth is evaluated for amplitude of GW signal of frequency f_{gw} while the noise PSD is evaluated at frequency $2f_{gw}$. This is because we are concentrating on the component of the product signal that is at (around) twice the frequency of the original signal (f_{gw}).

Chapter 3

Results & Discussions

In this chapter we state the results we obtain for our method of data analysis in the terms of the number of patches in the parameter space and sensitivity. We also make comparisons with respect to the earlier full coherent methods of data analysis of continuous gravitational waves ([2, 8]).

3.1 Choice of T_{sep}

We had explored two choices for T_{sep} to implement our method in order to cancel the doppler modulations. Our decision to use $T_{sep} = \frac{\pi}{\Omega}$ is based on the fact that this leads us to lesser number of patches that we need to search over in the parameter space. Let's assume a model in which

$$\omega_E = 366.25 \times \Omega$$

and there are no spin-downs for GW signal. For this model, considering the two choices of T_{sep}

- Canceling the orbital doppler (with some residual of the rotational doppler ($T_{sep} = \frac{\pi}{\Omega}$))

  In this case (ignoring the overall constant phase),

$$\Psi + \overline{\Psi} = 2\omega_{\rm gw} t + \phi(\omega_{\rm gw}, t) \tag{3.1}$$

where $\Psi \equiv \Psi(t)$ & $\overline{\Psi} \equiv \Psi(t + T_{sep})$ and,

$$\phi(\omega_{\rm gw}, t) = \frac{\omega_{\rm gw}}{c}(\vec{r}_{DE}(t) + \vec{r}_{DE}(t + T_{sep})) \cdot \hat{n} \tag{3.2}$$

The final expression for the product signal phase is:

$$\Psi + \overline{\Psi} = \Phi_0 + 2\omega_{\rm gw}t + \frac{\omega_{\rm gw}}{c}(r_p \cos\delta \cos(\omega_E t + \alpha + \chi)) \tag{3.3}$$

where,

$$r_p = \sqrt{2R_E^2(1 + \cos\omega_E T_{sep})} \cos\theta_l, \tag{3.4}$$

θ_l being the latitude location of the detector.

- Canceling the rotational doppler (with some residual of the orbital doppler ($T_{sep} = 183.5 days$)

  In this case,

$$\Psi + \overline{\Psi} = 2\omega_{\rm gw}t + \phi'(\omega_{\rm gw}, t) \tag{3.5}$$

  where

$$\phi'(\omega_{\rm gw}, t) = \frac{\omega_{\rm gw}}{c}(\vec{r}_{ES}(t) + \vec{r}_{ES}(t + T_{sep})) \cdot \hat{n} \tag{3.6}$$

  Here note that the terms with vectors $\vec{r}_{DE}$ are absent. This is because they are exactly canceled. This is what we call cancellation of rotational Doppler terms.

  The final expression for product signal phase is:

$$\Psi + \overline{\Psi} = \Phi_0 + 2\omega_{\rm gw}t + \frac{\omega_{\rm gw}}{c}(\tilde{r}' \cos n_\delta \sin(\Omega t + n_\alpha + \chi)) \tag{3.7}$$

  where, n_δ & n_α are the ecliptic latitude and longitude respectively, and:

$$r' = \sqrt{2R_o^2(1 + \cos\Omega T_{sep})} \tag{3.8}$$

From Fig. (3.2) & (3.1), it is apparent that the extent of doppler modulation is more for $T_{sep} = \frac{\pi}{\Omega}$ but the number of patches depends on r_p (r') as r_p^2 (r'^2) (section 3.6) and not directly on the extent of the doppler modulation. In the first case, r_p is of the order 10^4

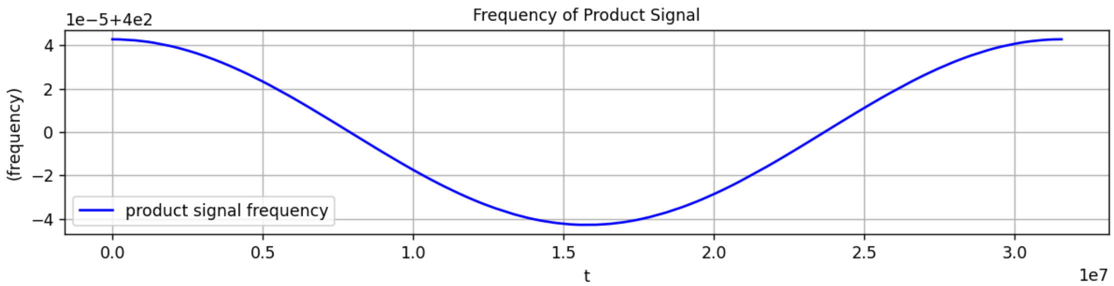

Figure 3.1: Plot of Frequency vs Time for $T_{sep} = 367 \times \frac{\pi}{\omega_E}$. The period of the modulations is a year.

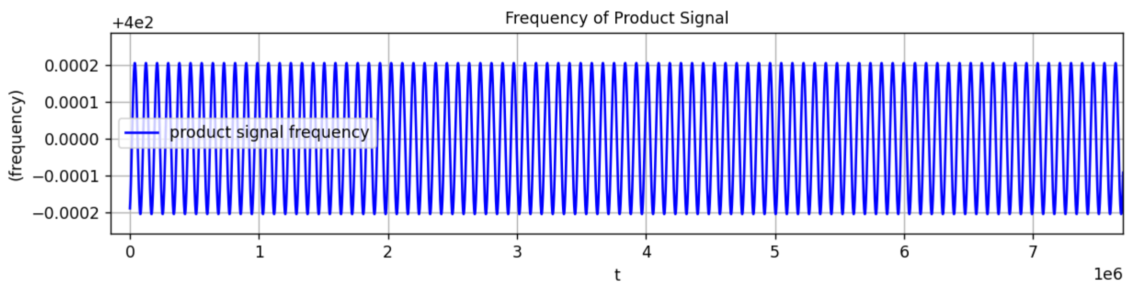

Figure 3.2: Plot of Frequency vs Time for $T_{sep} = \frac{\pi}{\Omega}$. The period of the modulation is a sidereal day.

while in the second case the corresponding distance r' is of the order 10^5 to 10^6. So, in the absence of spin-down terms, the number of patches required to be searched for is less in the case of $T_{sep} = \frac{\pi}{\Omega}$ compared to the other choice. This is the choice we have moved forward with.

3.2 Product signal in simple model

We consider the analytical form of the product signal for the model considered in 2.2.2. The choice of $\omega_E = N\Omega$ (odd N) makes sure that the doppler modulation completely gets canceled on multiplication of the signals temporally separated by $T_{sep} = \frac{\pi}{\Omega}$. Finally, the product signal has no Doppler frequency modulations but the amplitude modulations introduce fine side bands near double the GW frequency. We get the product signal $H(t;T)$ (the components near double the GW frequency) to be of the form:

$$H(t;T_0) \equiv h(t)h(t+T_0) = \sum_{k=-2}^{2} A_k \cos(\Psi + \overline{\Psi} + 2k\omega_E t) + B_k \sin(\Psi + \overline{\Psi} + 2k\omega_E t)\,, \qquad (3.9)$$

The coefficients in the equation (3.9) are known functions of the location and the orientation of the star and are described in appendix A. The sum of the signal phases comes out to be:

$$\Psi + \overline{\Psi} \equiv 2\omega_{\rm gw} t + \Psi_0 \qquad (3.10)$$

where,

$$\Psi_0 = \frac{\omega_{\rm gw}}{c}(\vec{r}_{DS}(t) + \vec{r}_{DS}(t+T)) \cdot \hat{n} + 2\Phi_0 + 2\Phi_0'\,. \qquad (3.11)$$

The quantity Ψ_0 is a constant because the vector sum inside the brackets results in a constant vector pointing along the axis of the rotation of the Earth. So this is how we get rid of the doppler modulation.

From (3.9), we can see that there would be five peaks in the power spectrum of the product signal. These peaks are very closely spaced, to be specific, at a difference of twice the frequency of the rotation of the Earth. These are a result of the amplitude modulation of the signal due to the periodicity of the antenna pattern functions.

Statistic to sum up the power in the peaks

We are also investigating the utility of statistic (3.12) for summing-up the power in the five peaks of the power spectrum of the signal.

$$c_T^2(\omega) = |\tilde{H}_T(\omega)|^2 + |\tilde{H}_T(\omega + 2\omega_E)|^2 + |\tilde{H}_T(\omega - 2\omega_E)|^2 + |\tilde{H}_T(\omega + 4\omega_E)|^2 + |\tilde{H}_T(\omega - 4\omega_E)|^2\,. \qquad (3.12)$$

where $\tilde{H}_T(\omega)$ is the finite time Fourier transform of the product signal $h(t) \times h(t+T)$).

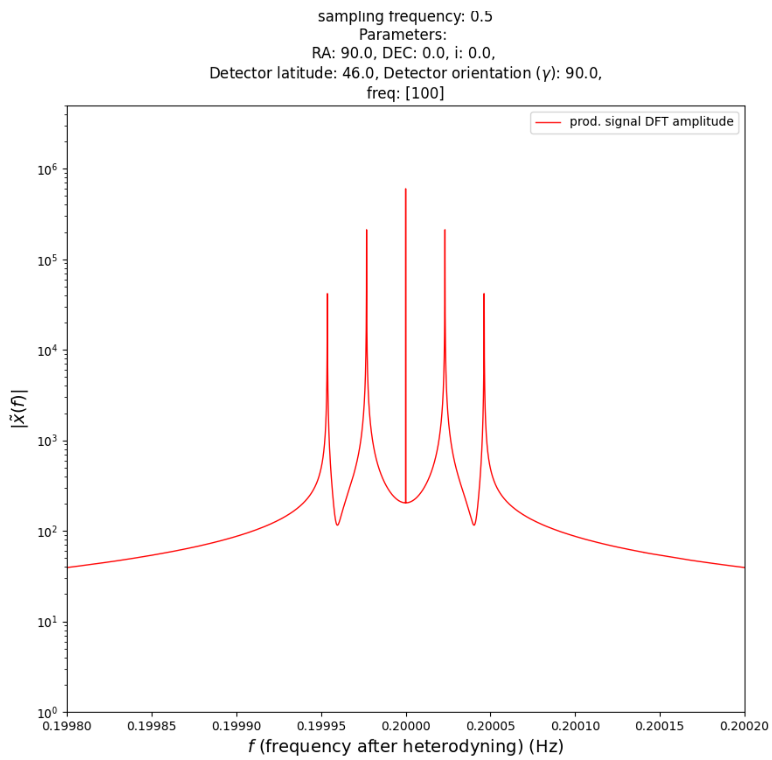

Figure 3.3: Amplitude spectrum of the signal for general model. Five peaks can be observed. The heterodyning frequency is lesser from the signal frequency by $0.1\,Hz$. So the heterodyned signal is at $\sim 0.2\,Hz$. The parameters taken for the signal are mentioned as the heading of the plot; γ is the angle made by the angle bisector of the detector arms with the West-East direction.

.

3.3 Product signal in general model

In case when the integral relation between the angular velocities Ω & ω_E does not hold, we have two choices for T_{sep} and as discussed in (3.1), we choose T_{sep} to be $\frac{\pi}{\Omega}$. This makes sure that we have lesser number of patches as compared to the other choice of T_{sep}. If we look at (3.3), the term containing $\cos(\omega_E t)$ oscillates many cycles in the period of ~ 6 months. That is why, the Fourier transform of the signal is given by Jacobi-Anger expansion. Thus many peaks would appear in the DFT of such a signal. The amplitude of DFT of the product signal with such a choice of T_{sep} is illustrated in Fig. (3.4). Note that these peaks appear without the demodulation of the signal.

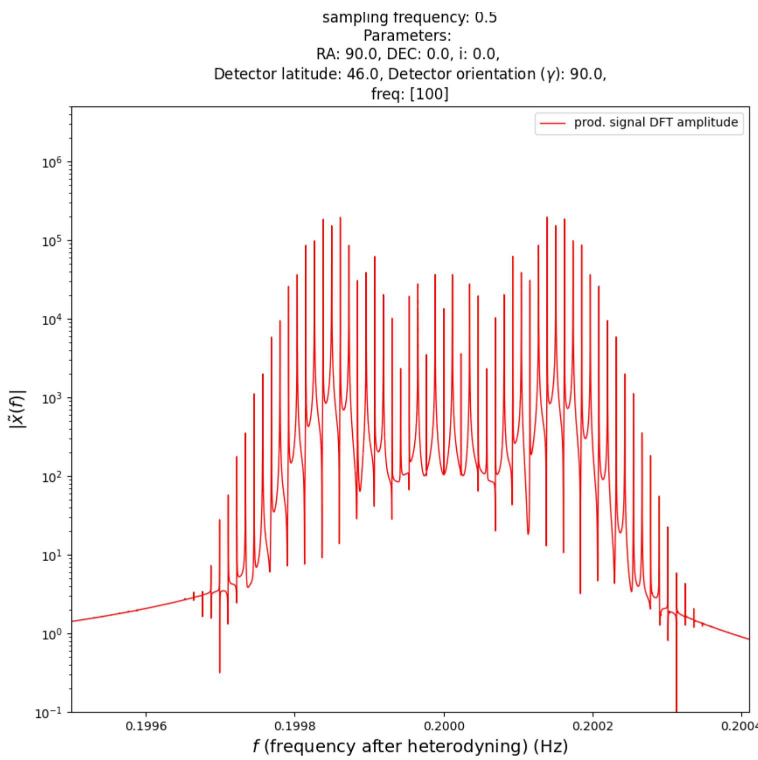

Figure 3.4: Amplitude spectrum of the signal for general model. Multiple peaks corresponding to Jacobi-Anger expansion can be observed .

.

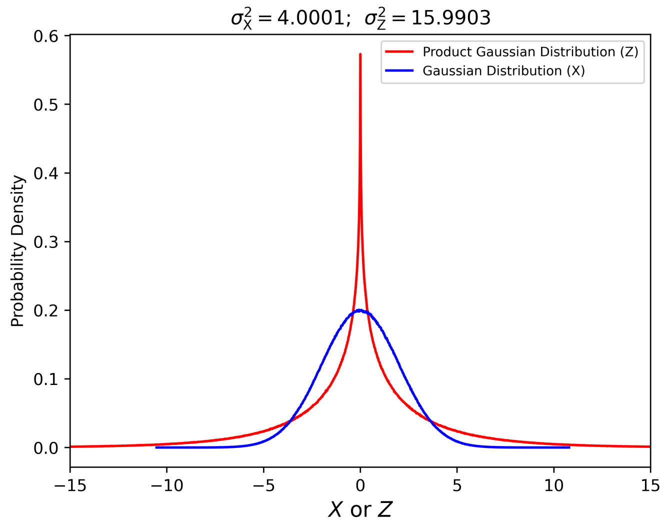

Figure 3.5: Probability distribution function of two random variables X and Z. X is normally distributed random variable, while Z is the product of two identical, non-correlated normally distributed random variables X and Y. This plot was created using 2×10^7 samples of identical non-correlated Gaussian random variables X and Y, each with variance $\sigma^2_{X \text{ or } Y} \approx 4$. The variance of random variable Z comes out to be ∼square of the variance of the individual normally distributed random variables.

3.4 Product Noise

Let's say that $n(t)$ represents the random variable for noise at time t. As over a narrow bandwidth, the PSD can be considered to be constant, it is safe to model the noise to be white. We have modeled the noise to be Gaussian with mean 0 and variance σ^2, i.e. $n(t) \sim \mathcal{N}(0, \sigma^2)$. Now, as we are multiplying two data streams, what we want to study is the distribution of random variable $n(t) \times n(t + T_{sep}) \equiv N(t)$. The two random variables $n(t) \equiv X$ and $n(t+T_{sep}) \equiv Y$ can be considered to be independent being separated by a long time. The distribution of random variable $Z \equiv XY$ does not remain Gaussian any longer ([5]). The probability distribution function of the random variable Z is given by

$$p(z) = \frac{K_0(|z|/\sigma^2)}{\pi\sigma^2}\,, \tag{3.13}$$

where K_0 is modified Bessel's function of the second kind. $N(t) \equiv Z$ has a variance of σ^4. See for illustration Fig. (3.5)

Distribution of the statistic

Even though the pdf of the product noise in time series is not Gaussian, the Fourier transform, i.e.

$$\tilde{N}_k = \sum_{j=0}^{N-1} N_j e^{-\frac{2\pi ijk}{N}}. \tag{3.14}$$

is still Gaussian by the central limit theorem ([12]). We have checked the validity of this claim numerically. Fig. (3.6) shows a Gaussian fit to the density histogram (labeled by 'data') of $\frac{\tilde{N}_k}{\sqrt{N}}$ where the DFT is divided by $\sqrt{N}$ for scaling it corresponding to the time series data. Here note that the original time series noise had a variance (σ^2) of 4. So the product noise would have a variance of 16. This is also (approximately) the sum of the variances of the two distributions in Fig. (3.6a) & Fig. (3.6b) (i.e. the imaginary and the real parts).

Now because the real and imaginary parts are both Gaussian, and the statistic we use is the power of the DFT, we can use the χ^2-statistic for the purpose of calculation of SNR and amplitude threshold calculations.

3.5 Demodulation Results

We can see (Fig. (3.7)) that demodulating reduces the number of peaks in the amplitude spectrum of the signal (compare Fig. (3.4) & Fig. (3.7)). There are 11 peaks all separated by the frequency of the rotation of the Earth. This is more than the number of peaks in the simple model case (section 3.2). To deal with this we can use a statistic similar to (3.12),

$$\begin{aligned} c_T^2(\omega) =& |\tilde{H}_T(\omega)|^2 + |\tilde{H}_T(\omega+\omega_E)|^2 + |\tilde{H}_T(\omega-\omega_E)|^2 + |\tilde{H}_T(\omega+2\omega_E)|^2 + |\tilde{H}_T(\omega-2\omega_E)|^2 + \\ & |\tilde{H}_T(\omega+3\omega_E)|^2 + |\tilde{H}_T(\omega-3\omega_E)|^2 + |\tilde{H}_T(\omega+4\omega_E)|^2 + |\tilde{H}_T(\omega-4\omega_E)|^2 + \\ & |\tilde{H}_T(\omega+5\omega_E)|^2 + |\tilde{H}_T(\omega-5\omega_E)|^2 . \end{aligned} \tag{3.15}$$

We need to investigate this further.

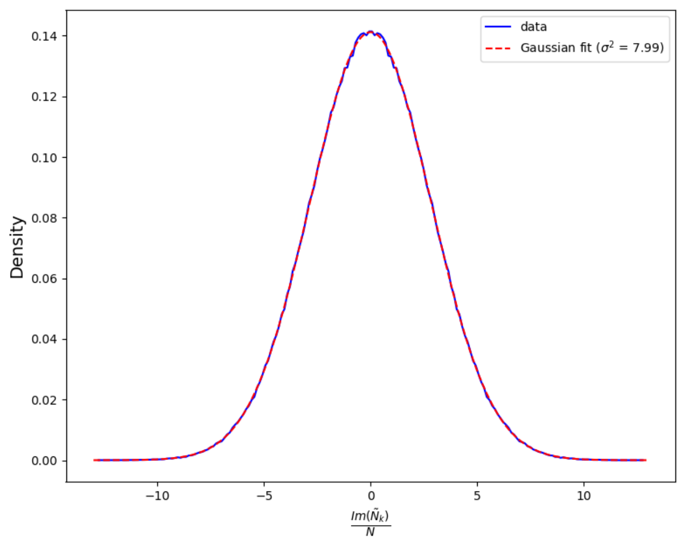

(a) Gaussian fit for the real part of $\frac{\tilde{N}_k}{\sqrt{N}}$

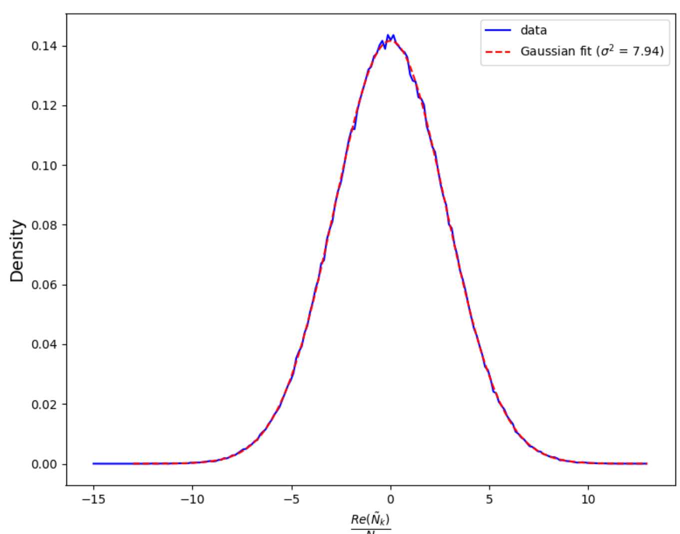

(b) Gaussian fit for the imaginary part of $\frac{\tilde{N}_k}{\sqrt{N}}$

Figure 3.6

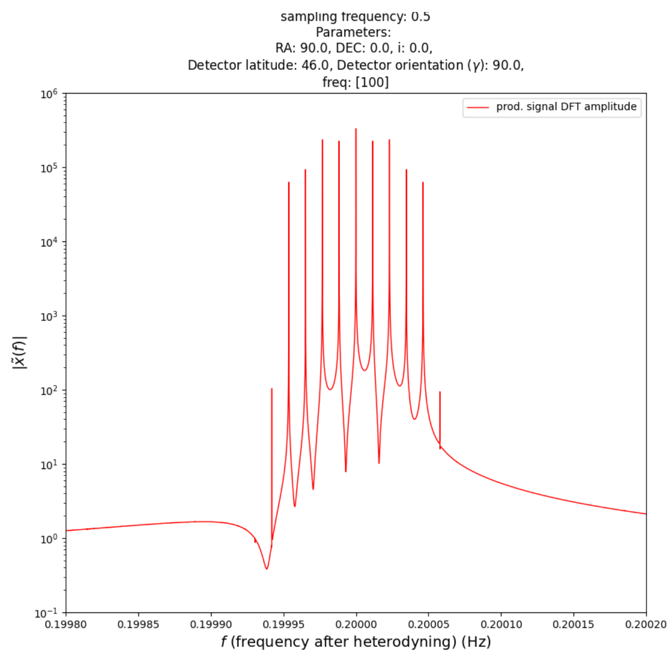

Figure 3.7: Amplitude spectrum of the signal for general model after resampling. Eleven peaks can be observed. All the consecutive peaks are separated by a frequency of the rotation of the Earth (i.e. $\frac{\omega_E}{2\pi}$).

.

3.6 Parameter Space Metric & Number of Patches

We have explored two cases:

- Signal with no spin-down
- Signal with one spin-down

The metric formalism and the methodology for our calculation is given in (2.4). We state the results for the number of patches in the parameter space required to be searched for, given a maximum mismatch.

3.6.1 Signals with no spin-downs

For signals with no spin-downs, the product signal phase is given by

$$\Psi_p(t;\vec{\mathbf{\Lambda}}) = 2\omega_{\rm gw}t + \frac{\omega_{\rm gw}}{c} r_p \cos\delta \cos(\omega_E t - \alpha + \tilde{\chi})\,, \tag{3.16}$$

where r_p is given by (3.4). The quantity $\omega_{\rm gw} r_p/c$ is actually $2\pi r_p/\lambda_{\rm gw}$, where $\lambda_{\rm gw}$ is the wavelength of the GW - it is essentially 2π times the the number of GW wavelengths that fit in r_p. We will denote it by n_λ and write,

$$n_\lambda = \frac{\omega_{\rm gw} r_p}{c} = \frac{2\pi r_p}{\lambda_{\rm gw}}\,. \tag{3.17}$$

The inverse of n_λ is in fact analogous to the resolution of the aperture or the "telescope".

Because of the simple form of the phase, it is easy to calculate the analytical forms of the metric (g and the projected metric Γ) elements. The elements of the metric g (2.23) are given by (T being the observation time)

$$g_{00} = \frac{T^2}{12}, \quad g_{11} = \frac{1}{2} n_\lambda^2 \cos^2\delta, \quad g_{22} = \frac{1}{2} n_\lambda^2 \sin^2\delta\,. \tag{3.18}$$

We do not consider the non diagonal elements as they don't scale with T and won't contribute to the projected metric for a long period of time ($T \gtrsim 100$ $days$).

So, the elements of the projected metric Γ (for $T \gtrsim 100$ $days$) are given by

$$\Gamma_{11} = \frac{1}{2} n_\lambda^2 \cos^2\delta, \quad \Gamma_{12} \approx 0, \quad \Gamma_{22} = \frac{1}{2} n_\lambda^2 \sin^2\delta\,, \tag{3.19}$$

From this we obtain

$$\det(\Gamma) = \frac{1}{4} n_\lambda^4 \cos^2\delta \sin^2\delta\,, \tag{3.20}$$

and integrating the square root of this over α and δ we obtain the parameter space area as:

$$A = \pi n_\lambda^2\,. \tag{3.21}$$

This turns out to be about ~ 1400 for $f_{gw} = 100$ Hz and $r_p = 10000 Km$, and it scales as square of f_{gw}. So, the number of patches corresponding to patch volume (2.26) and a maximum mismatch ($\hat{\mu}$) of 0.3 is ~ 1800. This is very less compared to the other full coherent methods that have been used earlier ([2], [7]) and hence our method is computationally more efficient. See for a comparison Fig. (3.8).

Fig. (3.8) is plotted using numerical implementation without ignoring any non diagonal metric elements; so it also shows that our approximations are correct; in fact the number of patches becomes nearly constant for $T \gtrsim 2$ day. We can say that the correlations (non-diagonal metric elements) matter only till an oscillation or two is completed. Here, the term $\cos(\omega_E t - \alpha + \tilde{\chi})$ in (3.16) oscillates with the same period as the Earth's rotation (1 sidereal day).

3.6.2 Signals with one spin-down

We consider another case of signals with one spin-down. This is good for certain kinds of low frequency continuous GW signals where one spin-down is sufficient to take into account the frequency evolution of the signal.([2]). The product signal phase is given by (2.16). For accessibility, we rewrite it here again

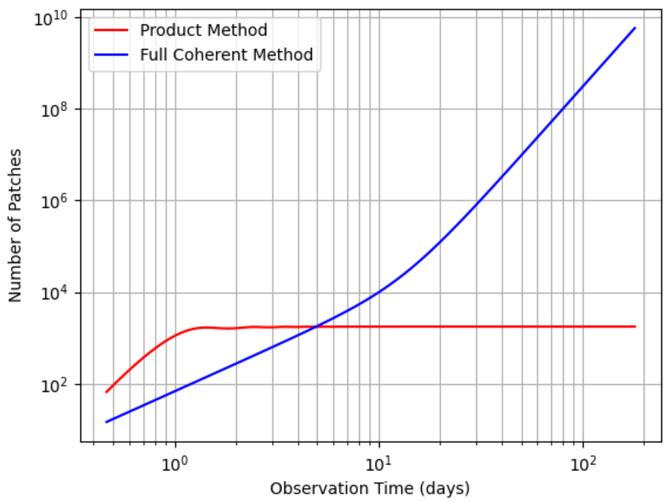

Figure 3.8: Comparison for the number of patches (as a function on observation time) required to be searched over in the sky for two methods. The "Product Method" is our method and the "Full Coherent" method is the method discussed in ([2] & [7]). We have assumed a maximum mismatch ($\hat{\mu}$) of 0.3 and a maximum frequency of $100Hz$ for both the methods for the purpose of calculation and comparison.

$$
\begin{aligned}
\Psi_p(t;\vec{\boldsymbol{\Lambda}}) \approx & 2\omega_{\text{gw}}t + \frac{\omega_{\text{gw}}}{c} r_p \cos\delta \cos(\omega_E t - \alpha + \tilde{\chi}) \\
& + \frac{\omega_{\text{gw}} f_1}{2}\left(2t^2 + 2T_{sep}t + T_{sep}^2 + \frac{2T_{sep}}{c} R_o \cos\delta \cos(\Omega t - \alpha + \chi')\right) + \Psi_0
\end{aligned}
\tag{3.22}
$$

As the analytical calculations are tedious, we simply state the numerical results as Fig. (3.9) in terms of the number of patches required to be searched for, given a maximum spin-down and a fixed observation time of ~ 6 months. The dependence of the number of patches on the observation time is very weak.

Note that the nature of the plot changes above spin-down magnitude of $\sim 10^{-10}\ Hz$ below which the curve follows a linear behavior, but later it turns to cubic with the spin-down parameter f_1. This nature can be explained by the second and the sixth term in (3.22). These terms are comparable in terms of their nature even though they oscillate at a completely different period, one with period of a sidereal day and the other with the period of a year. Ignoring the frequency differences, we see that the expressions that should be compared are (3.23)

$$r_p \ \& \ R_o T_{sep} f_1 \,. \tag{3.23}$$

When we equate the two terms, for $r_p = 10000\,Km$, we get $f_1 \sim 10^{-11}\,Hz$. This explains the behavior as the number of patches $\propto r_p^2$, but from (3.23), it should be $\propto f_1^2$ above $f_1 \sim 10^{-11}\,Hz$, and the linear dependence was already there from the integration. So finally we have the cubic dependence we observe in Fig. (3.9).

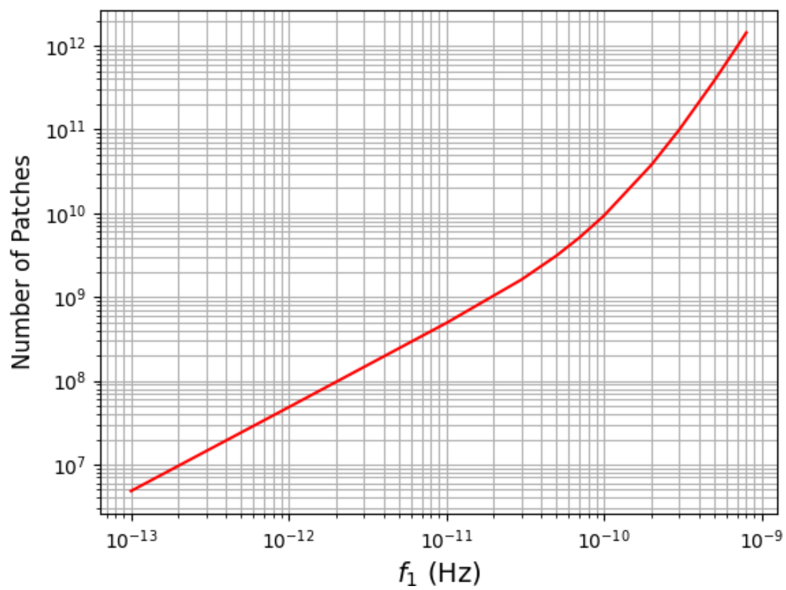

Figure 3.9: Plot for the number of patches as a function of maximum spin-down to be searched for. This is for a fixed observation time of $\sim$ 6 months and a maximum GW frequency of $100\,Hz$ (i.e. product signal frequency of $200\,Hz$).

Comparison with the earlier full-coherent methods

Fig. (3.10) shows a comparison for the number of patches for the two methods- our method, and the full-coherent method of ([2] & [7]) for a fixed observation time of $\sim$ 6 months. We see that the number of patches for the other method is significantly higher; in fact this many patches makes the search computationally difficult for an observation time of $\sim$ 6 months. More discussion on this is provided in the next section in the context of sensitivity of the searches.

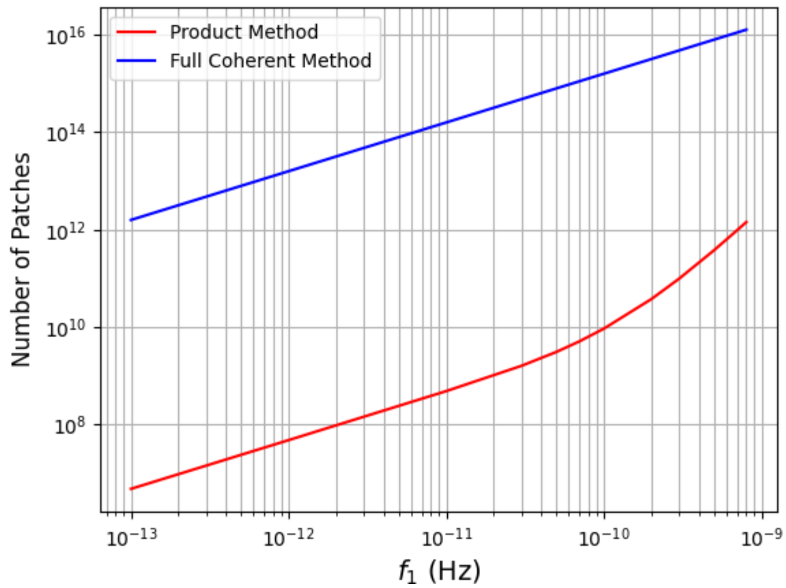

Figure 3.10: Plot for the comparison of the number of patches as a function of maximum spin-down to be searched for. This is for a fixed observation time of ~ 6 months and a maximum GW frequency of $100\,Hz$ (i.e. product signal frequency of $200\,Hz$).

3.7 Sensitivity Comparison

We compare the sensitivity of our method (product method) with the coherent methods ([2], [7]) using the depth of the searches (2.41 & 2.44). Due to quadratic noise, the depth for the product method ($\mathcal{D}_{th}^{prod}(f)$) is significantly less than the depth for the full coherent method ($\mathcal{D}_{th}(f)$) at a given frequency f and a fixed observation time.

We see that this is not a good comparison for the depths as the product signal is at twice the actual GW frequency f_{gw}.

Relative Depth

We define the relative depth of two methods as

$$\begin{aligned}\mathcal{D}^{rel}(f) &= \frac{\mathcal{D}_{th}^{prod}(2f)}{\mathcal{D}_{th}(f)}\sqrt{\frac{\mathbf{S}_f}{\mathbf{S}_{2f}}} \\ &= \frac{h_{th}(f_{gw}=f)}{h_{th}^{prod}(f_{gw}=f)}\end{aligned} \tag{3.24}$$

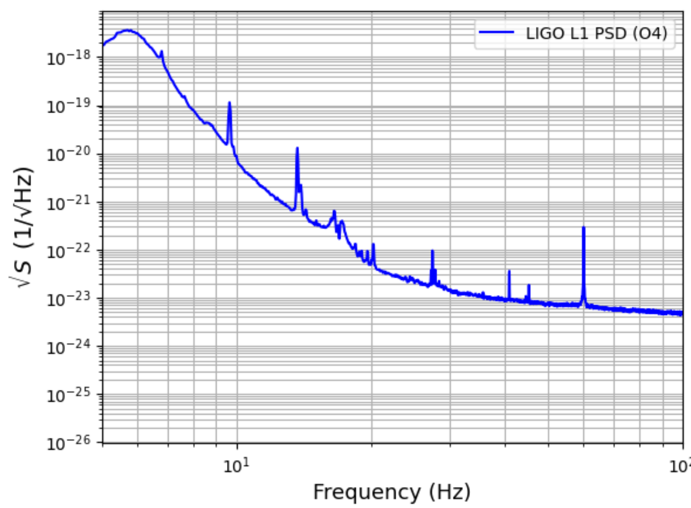

Figure 3.11: LIGO O4 noise PSD. This PSD was made from actual LIGO strain data[1] using Welch's method[2]. Note that the data might not be reliable below $10\,Hz$ so we don't make comments below this frequency.

We see that what matters is $\sqrt{\frac{\mathbf{S}_f}{\mathbf{S}_{2f}}}$ for a given detector. For LIGO, PSD has a large slope at lower frequency (Fig. 3.11, Fig. 3.12). This means we can have comparatively better sensitivity for low frequency signals. We have tested this claim for LIGO $O4$ run sensitivity curve.

We state the results for a fixed computational power of 1 Peta-FLOPs (10^{15} floating point operations per second). The full coherent method is computationally bounded so we calculate its sensitivity for an observation time corresponding to the bound on the computational

[1] `https://gwosc.org/eventapi/html/O4_Discovery_Papers/GW230529_181500/v1/`

[2] [9]

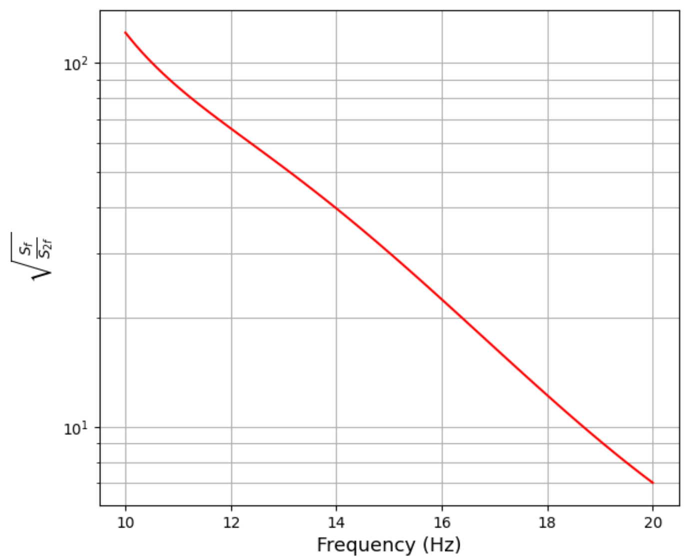

Figure 3.12: LIGO O4 noise PSD ratios. This plot was made using a smoothed out PSD curve corresponding to Fig. 3.11

. .

power. A plot for the maximum observation time as a function of maximum GW frequency to be searched for is given in Fig. (3.13) corresponding to the full-coherent method. For our method, we have considered a fixed observation time of ~ 6 months as computational cost is not a problem for this case, given a computational power of 1 Peta-FLOPs. The results for relative depth is given in Fig.(3.14). We can see that we are at an advantage compared to the full-coherent method for signals with frequencies below $17\,Hz$.

Comments on detection probability

Including the detection probability does not change the result by much. Without considering the detection probability, we are in advantage for signals with frequencies below $\sim 16.5\,Hz$. We need to be careful about including the detection probability to our results because when numerically implemented, the results vary significantly from the theoretical calculations ([13]).

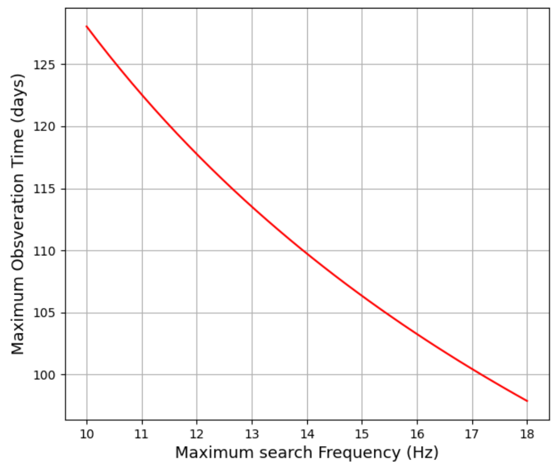

Figure 3.13: Limit on the observation time (for full-coherent method), given the maximum computational power of 1 Peta-FLOPs. The maximum spin-down was considered to be $8 \times 10^{-10}\,Hz$ (i.e. a spin-down time of 40 years).

.

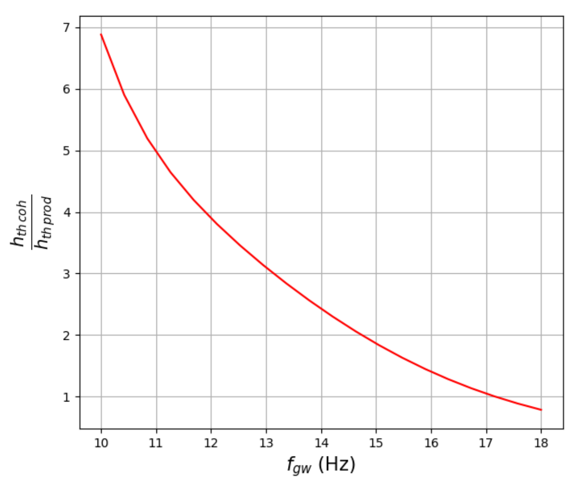

Figure 3.14: Relative depth for the two searches as a function of the GW signal frequency given a false alarm probability of 1%. Here we have also assumed a detection probability of 95% using non-central χ^2 -statistic.

.

Chapter 4

Conclusion

We see that our method performs significantly better in the low frequency band $(10 - 17\,Hz)$ for LIGO detectors while also being computationally inexpensive compared to the earlier methods. At the best, for a $10\,Hz$ signal, the sensitivity of our method is ~ 4.5 times the earlier full-coherent methods (given a minimum spin-down time of 40 years), and this remains higher till the frequency of $\sim 17Hz$. We present the comparison for the amplitude threshold corresponding to the mentioned frequency band in Fig.(4.1) for a false alarm probability of 1% and a detection probability of 95%.

Note that in these calculations we have ignored the effects of amplitude modulations which separates the single peak of the monochromatic signal into various. To deal with this we can use the statistics introduced in (3.15). With this, the only change that we will need to make in the sensitivity calculation would be the degrees of freedom of the χ^2-distribution and this won't change our results by much.

Remarks on actual orbit

It is well known that the Earth's orbit around the SSB is not perfectly circular but is nearly elliptical. In the case of elliptical orbits, there always exists a choice of T_{sep} that cancels the orbital Doppler modulation. If the orbit deviates from a perfect ellipse—for example, due to the Earth's motion around the Earth-Moon barycenter—the resulting Doppler modulation is small and has a negligible impact on the number of patches required to be searched over.

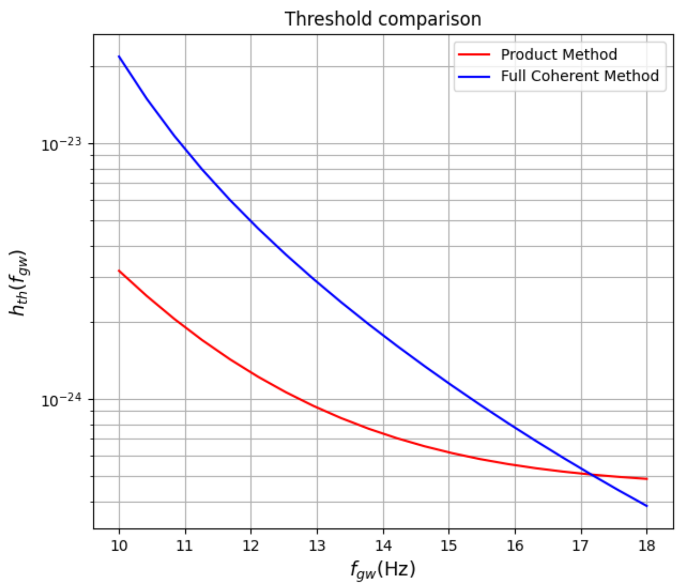

Figure 4.1: Amplitude threshold comparison for the two methods (given false alarm probability of 1% and detection probability of 95%).

.

We plan to extend our method to explicitly test the case of an elliptical orbit in future work.

Appendix A

The amplitudes describing the product signal in special case when $\omega_E = N \times \Omega$ (N being odd integer)

The amplitudes of the various terms in **??** are given in terms of the coefficients, which we present in four steps. First we define the functions:

$$
\begin{aligned}
\mathcal{C}_1(i,\delta,\theta_l,\gamma) &= 12(1+\cos^2 i)\cos^2\delta\cos^2\theta_l\sin 2\gamma,\\
\mathcal{C}_2(i,\delta,\theta_l,\gamma) &= (\cos 2\theta_l - 3)\sin 2\gamma(\cos 2\delta - 3)(1+\cos^2 i),\\
\mathcal{C}_3(i,\delta,\theta_l,\gamma) &= -4\sin 2\delta\sin 2\gamma\sin 2\theta_l(1+\cos^2 i),\\
\mathcal{C}_4(i,\delta,\theta_l,\gamma) &= -8\sin 2\delta\cos 2\gamma\cos\theta_l(1+\cos^2 i),\\
\mathcal{C}_5(i,\delta,\theta_l,\gamma) &= -4\cos 2\gamma(\cos 2\delta - 3)\sin\theta_l(1+\cos^2 i),\\
\mathcal{S}_1(i,\delta,\theta_l,\gamma) &= -32\cos^2 i\cos 2\gamma\cos\delta\cos\theta_l,\\
\mathcal{S}_2(i,\delta,\theta_l,\gamma) &= 32\cos^2 i\cos 2\gamma\sin\delta\sin\theta_l,\\
\mathcal{S}_3(i,\delta,\theta_l,\gamma) &= 16\cos^2 i\sin 2\gamma(2\cos\delta\sin 2\theta_l),\\
\mathcal{S}_4(i,\delta,\theta_l,\gamma) &= 8\cos^2 i(\cos 2\theta_l - 3)\sin\delta\sin 2\gamma.
\end{aligned}
\tag{A.1}
$$

The next set of functions is:

$$
\begin{aligned}
\mathcal{G}_{c0}(i,\delta,\theta_l,\gamma) &= \mathcal{C}_1^2 + \frac{1}{2}\{\mathcal{C}_2^2 + \mathcal{C}_5^2 + \mathcal{S}_1^2 + \mathcal{S}_3^2 - \mathcal{C}_3^2 - \mathcal{C}_4^2 - \mathcal{S}_2^2 - \mathcal{S}_4^2\}, \\
\mathcal{G}_{c1}(i,\delta,\theta_l,\gamma) &= 2\mathcal{C}_1\mathcal{C}_2 + \frac{1}{2}\{\mathcal{S}_1^2 + \mathcal{C}_4^2 - \mathcal{S}_3^2 - \mathcal{C}_3^2\}, \\
\mathcal{G}_{c2}(i,\delta,\theta_l,\gamma) &= \mathcal{C}_3\mathcal{C}_4 - \mathcal{S}_1\mathcal{S}_3 - 2\mathcal{C}_1\mathcal{C}_5, \\
\mathcal{G}_{c3}(i,\delta,\theta_l,\gamma) &= \frac{1}{2}(\mathcal{C}_2^2 + \mathcal{S}_4^2 - \mathcal{S}_2^2 - \mathcal{C}_5^2), \\
\mathcal{G}_{c4}(i,\delta,\theta_l,\gamma) &= \mathcal{S}_2\mathcal{S}_4 - \mathcal{C}_2\mathcal{C}_5,
\end{aligned}
\tag{A.2}
$$

$$
\begin{aligned}
\mathcal{G}_{s1}(i,\delta,\theta_l,\gamma) &= 2\mathcal{C}_1\mathcal{S}_2 - \mathcal{C}_3\mathcal{S}_1 + \mathcal{C}_4\mathcal{S}_3, \\
\mathcal{G}_{s2}(i,\delta,\theta_l,\gamma) &= \mathcal{C}_4\mathcal{S}_1 + \mathcal{C}_3\mathcal{S}_3 - 2\mathcal{C}_1\mathcal{S}_4, \\
\mathcal{G}_{s3}(i,\delta,\theta_l,\gamma) &= \mathcal{C}_2\mathcal{S}_2 - \mathcal{C}_5\mathcal{S}_4, \\
\mathcal{G}_{s4}(i,\delta,\theta_l,\gamma) &= -\mathcal{C}_5\mathcal{S}_4 - \mathcal{C}_2\mathcal{S}_4,
\end{aligned}
$$

Further, we define set of functions:

$$
\begin{aligned}
A_0 &= 2K\mathcal{G}_{c0}, \\
B_0 &= 0 \\
A_{1c\pm} &= K(\mathcal{G}_{c1} \pm \mathcal{G}_{s2}), \\
A_{1s\pm} &= K(\mathcal{G}_{c2} \mp \mathcal{G}_{s1}), \\
B_{1c\pm} &= K(\mathcal{G}_{s1} \mp \mathcal{G}_{c2}), \\
B_{1s\pm} &= K(\mathcal{G}_{s2} \pm \mathcal{G}_{c1}), \\
A_{2c\pm} &= K(\mathcal{G}_{c3} \pm \mathcal{G}_{s4}), \\
A_{2s\pm} &= K(\mathcal{G}_{c4} \mp \mathcal{G}_{s3}), \\
B_{2c\pm} &= K(\mathcal{G}_{s3} \mp \mathcal{G}_{c4}), \\
B_{2s\pm} &= K(\mathcal{G}_{s4} \pm \mathcal{G}_{c3}),
\end{aligned}
\tag{A.3}
$$

where,

$$
K = \frac{h_0^2}{4096} \tag{A.4}
$$

Finally, we define the coefficients in the equation **??** as:

$$
\begin{aligned}
A_0 &= 2K\mathcal{G}_{c0} \\
B_0 &= 0 \\
A_{\pm 1} &= \{A_{1c\pm}\cos 2\alpha + A_{1s\pm}\sin 2\alpha\} \\
B_{\pm 1} &= \{B_{1c\pm}\cos 2\alpha + B_{1s\pm}\sin 2\alpha\} \\
A_{\pm 2} &= \{A_{2c\pm}\cos 4\alpha + A_{2s\pm}\sin 4\alpha\} \\
B_{\pm 2} &= \{B_{2c\pm}\cos 4\alpha + B_{2s\pm}\sin 4\alpha\}
\end{aligned}
\tag{A.5}
$$

The coefficient B_0 is zero because of the choice of the coordinates and initial phases of the rotation of the Earth.

Appendix B

Comparison of number of patches calculated for barycentric resampling method and F-statistic method

Here we compare the results of number of patches (filters) required be searched for for two methods- barycentric resampling method as in ([2]) and the F-statistic method as in ([8]).

We will only consider one spindown case as this is also the maximum spindown we have considered in this work. We assume that the analytical results given in Eqs. (6.3) to (6.7) of ([2]) are true till observation time of 20 to 30 days as it is mentioned there that the results were derived by numerically fitting analytical function to plot they have given for a maximum observation time of $\sim$ 20 days. For the F-statistic method, the calculations are much simpler due to linearized phase as in ([7]). So we have recalculated the metric and number of patches are scaled according to the volume of patch as given in ([2]). This lets us compare the number of patches for the two methods. The results for mentioned maximum spindown and maximum frequency can be seen in Fig. (B.1).

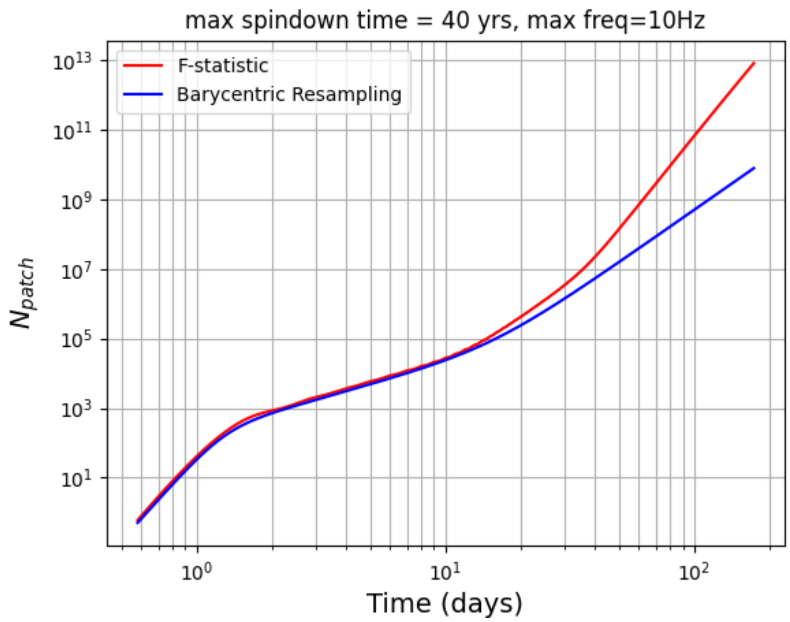

Figure B.1: Plot for Comparison of number of patches in barycentric resampling method and F-statistic method

We can see that there's a very good match of number of patch for the two cases for ~ 20 days. This is what we expect for the reasons mentioned above.

Bibliography

[1] R. Balasubramanian, B. S. Sathyaprakash, and S. V. Dhurandhar. “Gravitational waves from coalescing binaries: detection strategies and Monte Carlo estimation of parameters”. In: *Physical Review D* (1996). DOI: 10.1103/PhysRevD.53.3033.

[2] P. R. Brady et al. “Searching for periodic sources with LIGO”. In: *Physical Review D* (1998). DOI: 10.1103/PhysRevD.57.2101.

[3] Patrick R. Brady and Teviet Creighton. “Searching for periodic sources with LIGO. II. Hierarchical searches”. In: *Phys. Rev. D* (2000). DOI: 10.1103/PhysRevD.61.082001.

[4] S. Dhurandhar and S. Mitra. *General Relativity and gravitational waves*. Springer, 2022.

[5] Sanjeev Dhurandhar et al. “Cross-correlation search for periodic gravitational waves”. In: *Physical Review D* (2008). DOI: 10.1103/PhysRevD.77.082001.

[6] Sanjeev V. Dhurandhar and Alberto Vecchio. “Searching for continuous gravitational wave sources in binary systems”. In: *Physical Review D* (2001). DOI: 10.1103/PhysRevD.63.122001.

[7] Piotr Jaranowski and Andrzej Krolak. “Data analysis of gravitational-wave signals from spinning neutron stars. III. Detection statistics and computational requirements”. In: *Phys. Rev. D* (2000). DOI: 10.1103/PhysRevD.61.062001.

[8] Piotr Jaranowski, Andrzej Królak, and Bernard F. Schutz. “Data analysis of gravitational-wave signals from spinning neutron stars. I. The signal and its detection”. In: *Physical Review D* (1998). DOI: 10.1103/PhysRevD.58.063001.

[9] Alex Nitz et al. *Gwastro/pycbc: V2.3.3 Release of Pycbc*. Jan. 2024. DOI: 10.5281/zenodo.10473621.

[10] Reinhard Prix. "Template-based searches for gravitational waves: efficient lattice covering of flat parameter spaces". In: *Classical and Quantum Gravity* (2007). DOI: `10.1088/0264-9381/24/19/S11`.

[11] Keith Riles. "Searches for Continuous-Wave Gravitational Radiation". In: *Living Reviews in Relativity* (2023). DOI: `10.1007/s41114-023-00044-3`.

[12] Massimo Tinto. "A Fast Data Processing Technique for Continuous Gravitational Wave Searches". In: *Universe* (2021). DOI: `10.3390/universe7120486`.

[13] Karl Wette. "Estimating the sensitivity of wide-parameter-space searches for gravitational-wave pulsars". In: *Physical Review D* (2012). DOI: `10.1103/PhysRevD.85.042003`.